Check for updates

Mechanism of auto-inhibition and activation of Mec1ATR checkpoint kinase

Elias A. Tannous [1,3], Luke A. Yates [2,3], Xiaodong Zhang [2 ✉] and Peter M. Burgers [1 ✉]

In response to DNA damage or replication fork stalling, the basal activity of Mec1ATR is stimulated in a cell-cycle-dependent manner, leading to cell-cycle arrest and the promotion of DNA repair. Mec1ATR dysfunction leads to cell death in yeast and causes chromosome instability and embryonic lethality in mammals. Thus, ATR is a major target for cancer therapies in homologous recombination–deficient cancers. Here we identify a single mutation in Mec1, conserved in ATR, that results in constitutive activity. Using cryo-electron microscopy, we determine the structures of this constitutively active form (Mec1(F2244L)-Ddc2) at 2.8 Å and the wild type at 3.8 Å, both in complex with Mg^{2+}-AMP-PNP. These structures yield a near-complete atomic model for Mec1–Ddc2 and uncover the molecular basis for low basal activity and the conformational changes required for activation. Combined with biochemical and genetic data, we discover key regulatory regions and propose a Mec1 activation mechanism.

The cell-cycle checkpoint machineries constitute important pathways that coordinate DNA damage and replication challenges with DNA repair and cell-cycle progression. The initiating protein kinases ATM and ATR, yeast Tel1 and Mec1, respectively, show great promise as targets for drugs in anticancer treatment[1]. These two kinases play broad and complex regulatory roles, not just in situations of replication stress or DNA damage, but also during normal cell-cycle progression. However, our current structural, biochemical and mechanistic understanding of these enzymes remains poor, hindering our understanding of DNA damage response processes and effective therapeutic intervention.

Yeast Mec1 (hATR) belongs to the family of phosphatidylinositol-3-kinase-related kinases (PIKK), which also include yTel1 (hATM), yTor1, 2 (mTOR) and DNA-PKcs[2]. Both Mec1ATR and Tel1ATM show a basal protein kinase activity that is stimulated by specific activator proteins in response to DNA damage or replication stress[3–10]. Three activators have been identified, which stimulate Mec1 activity in a cell-cycle-specific manner[11,12] (Fig. 1a). Mec1 and its integral partner Ddc2 (hATRIP) exist in a stable complex as a dimer of heterodimers[13,14]. Ddc2 contributes to the stability of the complex through Ddc2–Ddc2 dimerization[15] and Ddc2-Mec1 interactions, and directs Mec1 to the site of damage through its direct interaction with the single-strand DNA-binding protein RPA[16]. Ddc2 is also regulated by phosphorylation and its degradation contributes to checkpoint adaptation[17].

The kinase domains of PIKKs contain a number of highly conserved functional motifs found in almost all kinases; these include a Glycine-rich loop (G-loop), a catalytic loop that harbors residues responsible for Mg^{2+}-ATP binding, catalysis and phosphoryl transfer (for example, the highly conserved HRD motif, which is DRH in PIKKs), and a Mg^{2+}- and peptide-binding activation loop that usually contains a DFG motif, with minor variability in PIKKs (DLG, DFD, DFN) (Fig. 1b,c). The DFG-Asp is invariant and responsible for chelating the magnesium required for catalysis[18]. The DFG-Phe is highly conserved, with the exception of Tel1ATM in which it is replaced by a Leu (Fig. 1c), while the Gly is replaced by an Asp in Mec1 or Asn in ATR. A distinct feature of the PIKK family is a

region referred to as the PRD (PIKK regulatory domain), which is thought to play a role in regulating the catalytic activity by mediating interactions with other proteins[5,19,20] and regulating protein substrate access[21]. PIKKs also have variable lengths of N-terminal HEAT repeats followed by a conserved FAT domain. Various roles for these additional domains have been elucidated in the last few years through structural and biochemical studies[22–24].

An integrated mutational analysis of Mec1ATR and PIKKs in general by both biochemical and genetic methodologies has been scarce. Point mutations in the Mec1 catalytic residues Asp2224 and Asp2243, which coordinate Mg^{2+}, show a phenotype similar to that of the *mec1Δ* mutant[25,26]. A point mutation in the PRD region of human ATR, Lys2589 (Lys2326 in Mec1) was shown to affect the activation by TopBP1 (the ortholog of yeast Dpb11)[5]. Recent cryo-EM structures of Mec1–Ddc2 and ATR–ATRIP have revealed some of the key interactions[27,28]. However, the structural models of Ddc2 and ATRIP were not fully resolved in those structures and there are a number of discrepancies between the cryo-EM structure of Mec1–Ddc2 and that of the crystal structures of the domain containing the Ddc2 coiled-coil and RPA-interacting sites[15,29]. Furthermore, these studies do not address how the kinase activity of Mec1 is maintained in a basal state and what conformational changes are required to stimulate its activity.

The activation loop of PIKKs is widely conserved in eukaryotes. It shares homology with other protein kinases and can undergo large conformational changes when switching from inactive to active states[30]. In Mec1, the activation loop spans between residues H2241 and R2263, containing 2243DFD2245 (Fig. 1c and Extended Data Fig. 1d). Close to the activation loop is a poorly conserved loop (2309DRNMDHSIQ2317), which is flanked by two α-helices. In a recent structural comparison of several PIKKs, including Mec1 and Tel1, this region has been designated PRD-I (PRD Insertion), which is proposed to be key in maintaining Tel1ATM in an inhibited state through blocking substrate access[21]. Here, using an integrated biochemical and genetic analysis for checkpoint function, we identified a number of mutations in the activation loop and the PRD-I that have profound effects on its activity. Remarkably,

[1]Department of Biochemistry and Molecular Biophysics, Washington University School of Medicine, Saint Louis, MO, USA. [2]Section of Structural Biology, Department of Infectious Disease, Imperial College London, South Kensington, London, UK. [3]These authors contributed equally: Elias A. Tannous, Luke A. Yates. ✉e-mail: xiaodong.zhang@imperial.ac.uk; burgers@wustl.edu
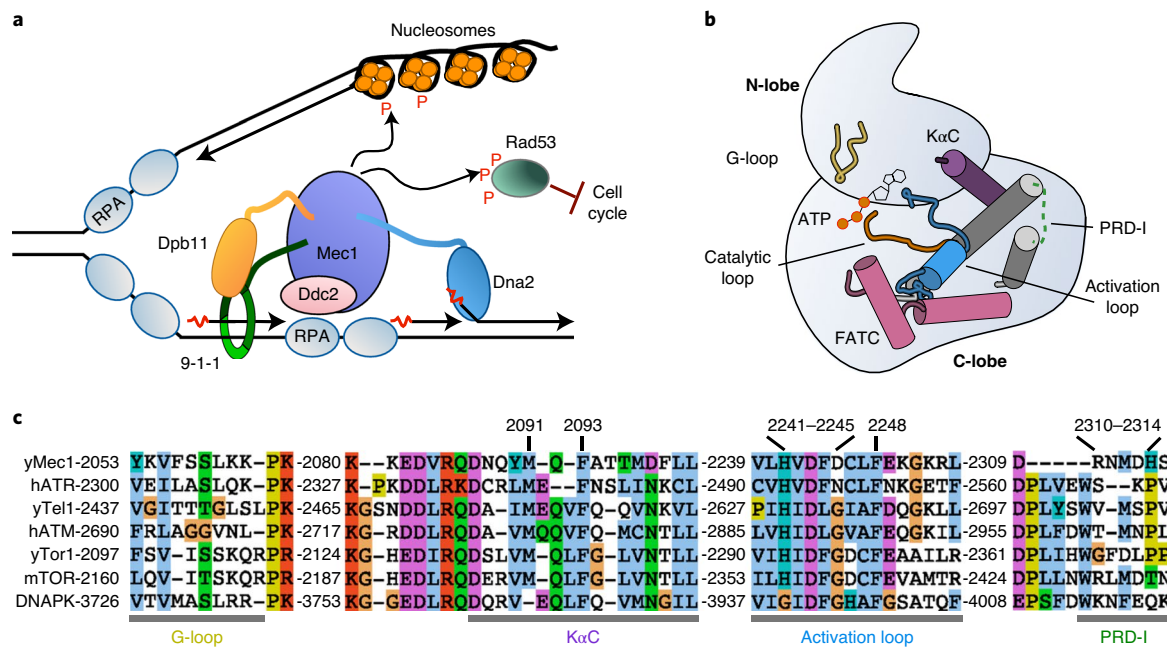
Fig. 1 | Model of Mec1[ATR] function and PIKK activation. a, Simplified model of the yeast DNA replication fork and replication stress response through Mec1–Ddc2 and its activators. The yeast activators shown are the Ddc1[Rad9] subunit of the 9-1-1 checkpoint clamp, the replication initiator protein Dpb11[TopBP1] and the nuclease–helicase Dna2. These three proteins have an unstructured C-terminal domain (Ddc1, Dpb11) or N-terminal domain (Dna2), which mediates activation. **b**, Structural model of relevant helices and loops of the Mec1 kinase domain. **c**, Sequence alignment of yeast Mec1 and human ATR with other members of the PIKK class, representing the regions and specific residues targeted in this study. The PRD-I residues were realigned based on structural conservation.

we find that a single substitution in the DFD motif, F2244L, results in constitutive activity in vitro. This mutant can rescue the lethality of a yeast mutant deficient for all activators of Mec1. To corroborate these mutagenesis studies, we determined the structures of the AMP-PNP-bound form (a nonhydrolyzable analog of ATP) of wild-type Mec1–Ddc2 and Mec1(F2244L)–Ddc2 by cryo-EM at 3.8-Å and 2.8-Å resolution, respectively. Together, our results explain how Mec1–Ddc2 maintains minimal basal activity and the structural basis for its activation. Furthermore, these structures, together with our genetic and biochemical data, explain the unique property of the DFD motif and other key functional regions, and suggest a robust model of how Mec1[ATR] is activated.

Results

The activation loop regulates Mec1 basal activity. We constructed, overproduced and purified 25 Mec1 point mutants that yielded homogeneous heterodimeric Mec1–Ddc2 complexes, similar to wild type (Methods). We compared the basal protein kinase activity of these mutants with wild-type and their activity when stimulated by the Dpb11[TopBP1] activator. Additionally, we used a second Mec1 activator, the nuclease-helicase Dna2, which is involved in DNA replication and DNA repair, but in addition has an S-phase-specific replication checkpoint function, residing in its N-terminal domain (NTD; 1–499)[31]. This Dna2 domain was used to query whether the Mec1 mutants showed defects that were dependent on the type of activator. Rad53 checkpoint kinase, the major target of Mec1 during checkpoint initiation, was used as the phosphorylation target. Basal Mec1 kinase assays (without activator) were carried out at both 40 and 100 mM NaCl to separate effects on nucleotide and Mg²⁺ binding, as higher salt is shown to eliminate weak Mg²⁺ binding[32]. All kinase assays with activator were carried out at 100 mM NaCl, which is the optimal salt concentration for wild-type Mec1 (ref. [6]). Using a complementary genetic analysis, we tested the equivalent *mec1* mutants for their

effects on growth, sensitivity to the replication inhibitor hydroxyurea and sensitivity to DNA-damaging agents in several indicator strains that are progressively compromised for the cell-cycle checkpoint circuitry.

We first targeted the activation loop for mutagenesis. Mutation of either H2241 or V2242, which are conserved in ATR and other PIKKs, led to a sharp reduction of Mec1 activity (Fig. 2a–c). Mutation of D2243 to Asn was phenotypically similar to *mec1Δ* and the purified mutant showed no kinase activity, similar to previous reports[25,26]. We also targeted the highly conserved F2248 in the activation loop for mutagenesis. Mec1(F2248A) showed reduced basal activity and activation by Dpb11 (Fig. 2a–c).

To test the phenotypes of these mutants, we used a centromere plasmid shuffle technique to replace wild-type *MEC1* with each of the *mec1-x* mutants in a *mec1Δ* strain. In addition, we used progressively checkpoint-compromised strains, defective for the second checkpoint kinase Tel1[ATM] (*tel1Δ*), or in addition for Ddc1 (*tel1Δ ddc1Δ*). Ddc1 is a subunit of the 9-1-1 (Ddc1-Rad17-Mec3, human Rad9-Rad1-Hus1) checkpoint clamp[33,34]. In the *ddc1Δ* mutant, the checkpoint functions of both 9-1-1 and Dpb11 (human TopBP1) are defective[7], leaving only Dna2 as S-phase-specific Mec1 activator[8].

The *mec1-H2241A*, *mec1-V2242A* and *mec1-F2248A* mutants, which showed 70–90% reduction in kinase activity, showed defects under unchallenged growth conditions, and sensitivity to growth on hydroxyurea. These strains showed exquisite sensitivity to hydroxyurea when the checkpoint circuitry was progressively compromised in the *tel1Δ* and *tel1Δ ddc1Δ* genetic backgrounds (Fig. 2d), thus establishing a direct correlation between in vitro kinase activity and in vivo growth and hydroxyurea sensitivity.

A surprising function of F2244 in the DFD motif. Central in the activation loop is the highly conserved F2244 of DFD, which we mutated to Ala, and also Leu because Tel1[ATM] has Leu at that position (Fig. 1c). F2244A and F2244L Mec1–Ddc2 proteins showed
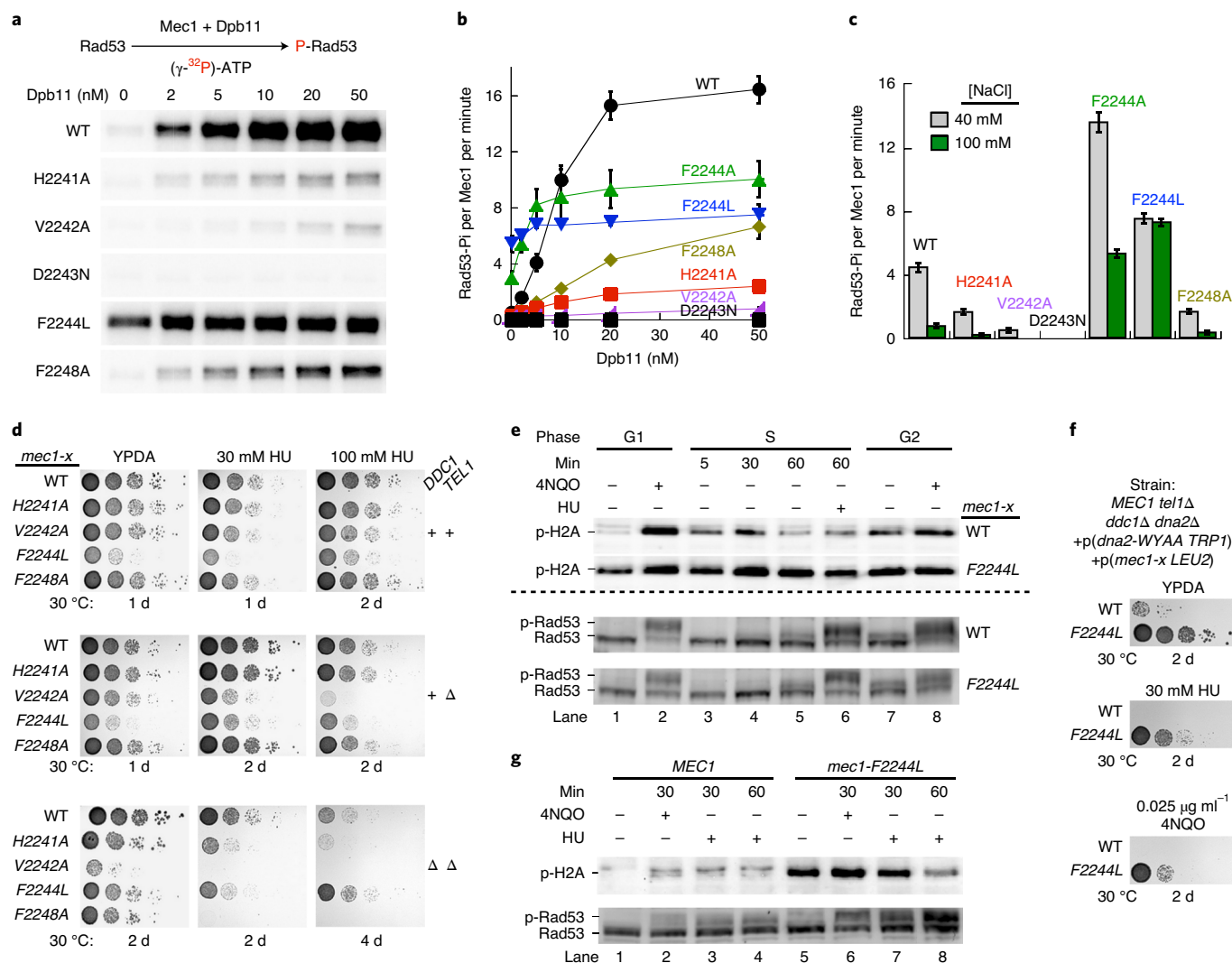
Fig. 2 | Activation loop mutagenesis of Mec1. a, Phosphorylation of Rad53 by Mec1 or Mec1-x mutants with the indicated concentrations of Dpb11 activator. To eliminate contributions by Rad53 kinase itself, the kinase-dead version was used (Rad53-kd, K227A). An example of a full gel is shown in Extended Data Fig. 1a. Uncropped gel images are shown in the source data. **b**, Quantification of the data in **a** and of analogous assays with the indicated mutants. Activities are expressed as Rad53 phosphates per Mec1 (monomer) per minute. **c**, Phosphorylation of Rad53 in the absence of Dpb11 (Mec1 basal activity), with either 40 mM or 100 mM final NaCl. **d**, Growth of *MEC1* mutants. Strains PY405, PY406 and PY414 are *mec1Δ* and contain plasmid p(*LEU2 mec1-x*). *TEL1* and *DDC1* status are shown on the right. The strains were tested for growth on yeast peptone dextrose agar (YPDA) plates with or without hydroxyurea, as indicated. **e**, Western blot analysis of phospho-H2A (pS129) (top) and Rad53 (bottom) in *tel1Δ* strain PY406, with either wild-type *MEC1* or *mec1-F2244L*. Cells were arrested in G1 phase with alpha-factor, or in G2 phase with nocodazole, or were arrested in G1 phase with alpha-factor and released into S-phase with or without 200 mM hydroxyurea. G1-arrested or G2-arrested cells were treated with 4NQO for 30 min where indicated (Methods). Ponceau staining of the blot is shown in Extended Data Fig. 1f. **f**, Growth of activator-defective *MEC1* strain, with the relevant genotype shown, on media with or without 4NQO (0.025 μg ml⁻¹) or 30 mM hydroxyurea (Extended Data Fig. 2b). **g**, Western blot analysis of the same strains. Asynchronously growing cells were treated with 2 μg ml⁻¹ 4NQO or 200 mM hydroxyurea for the indicated times. Ponceau staining of the blot is shown in Extended Data Fig. 2c. Error bars for panels **b** and **c** represent the mean ± s.e.m. of *n* = 3 independent assays. Uncropped blot images of panels **a,e,g** and data for graphs in panels **b** and **c** are reported as source data. HU, hydroxyurea; WT, wild type.

unusual high basal activity, ~10-fold and ~20-fold higher for the F → A and F → L mutants, respectively. For our further studies, we selected Mec1(F2244L), which showed the highest basal activity at 100 mM NaCl and only minimal activation by Mec1 activators. Indeed, activation of Mec1(F2244L) by Dpb11 and Dna2(1–499), or a small peptide derived from Dna2 (ref. [8]), was less than 1.5-fold (Fig. 2a–c and Extended Data Fig. 1b,c). However, the fully activated mutant enzyme showed only half the activity of activated wild-type Mec1 (Fig. 2b). In a control assay, we showed that the increase in basal activity was not due to an enhanced affinity of the mutant enzyme for the substrate, Rad53 (Extended Data Fig. 1e).

We replaced *MEC1* with the constitutive active allele *mec1-F2244L*. In wild-type yeast, this mutation exhibited slow growth (Fig. 2d, top panels). Interestingly, in the checkpoint-compromised *tel1Δ ddc1Δ* mutant background, *mec1-F2244L* showed slightly increased growth over wild type on 100 mM hydroxyurea (Fig. 2d, bottom panels). The poor growth of *mec1-F2244L* in wild-type yeast could be due to gratuitous, damage-independent phosphorylation of key cell-cycle factors, which can affect progression of the cell cycle. Indeed, a cell cycle analysis of the mutant shows that it progressed more slowly through S-phase (Extended Data Fig. 2d). Surprisingly, *mec1-F2244L* showed little or no increased phosphorylation of

Table 1 | Cryo-EM data collection, refinement and validation statistics

	Mec1(F2244L)–Ddc2 (AMP-PNP-bound State I) (EMD-11050, PDB 6Z2W)	Mec1(F2244L)–Ddc2 (AMP-PNP-bound State II) (EMD-11051, PDB 6Z2X)	AMP-PNP Mec1–Ddc2 (EMD-11055, PDB 6Z3A)	Mec1–Ddc2 (EMD-11056)
Data collection and processing				
Magnification	81,000	81,000	81,000	75,000
Voltage (kV)	300	300	300	300
Electron exposure (e$^-$/Å^2)	51	51	44	59
Defocus range (μm)	−1.5 to −3.0	−1.5 to −3.0	−0.8 to −2.5	−2.0 to −3.8
Pixel size (Å)	1.06 (0.53 super resolution)	1.06 (0.53 super resolution)	1.06 (0.53 super resolution)	1.09
Tilt angle (°)	0	0	0	0, −30
Symmetry imposed	C2	C2	C2	C2
Initial particle images (no.)	~0.9 million	~0.9 million	~1.9 million	~2.0 million
Final particle images (no.)	53,581	12,205	26,180	132,193
Map resolution (Å)	2.8	3.2	3.8	4.3
FSC threshold	0.143	0.143	0.143	0.143
Map resolution range (Å)	2.5–3.7	2.7–3.9	3.5–5.0	3.5–5.0
Refinement				
Initial model used	PDB 5X6O, PDB 4JSP, PDB 6S8F	PDB 6Z2W	PDB 6Z2W	
Model resolution (Å)	3.0	3.5	4.5	
FSC threshold	0.5	0.5	0.5	
Model resolution range (Å)	2.5–3.7	2.7–3.9	3.5–5.0	
Map sharpening B factor (Å^2)	−20 to −40	−20 to −60	−40 to −80	
Model composition				
Nonhydrogen atoms	46,588	46,604	46,142	
Protein residues	5,766	5,766	5,730	
Ligands	2 AMP-PNP, 4 Mg^{2+}, 2 Zn^{2+}	2 AMP-PNP, 4 Mg^{2+}, 2 Zn^{2+}	2 AMP-PNP, 2 Zn^{2+}	
B factors (Å^2)				
Protein	57.1	77.4	260.5	
Ligand	99.3	110.2	323.1	
R.m.s. deviations				
Bond lengths (Å)	0.008	0.007	0.007	
Bond angles (°)	1.4	1.1	1.3	
Validation				
MolProbity score	1.83	1.80	2.13	
Clashscore	6.0	5.6	10.6	
Poor rotamers (%)	0.8	0.46	1.04	
Ramachandran plot				
Favored (%)	91.54	91.76	88.84	
Allowed (%)	8.46	8.20	11.7	
Disallowed (%)	0.00	0.03	0.1	

Rad53, the major downstream effector in DDR and replication stress, unless cells were challenged with DNA damage or hydroxyurea (Fig. 2e)[35–37]. Thus, it appears that slow growth of the mutant is not caused by gratuitous, canonical checkpoint activation. To investigate another possible target of *mec1-F2244L*, we probed the phosphorylation status of histone H2A. S129 of H2A is a target for Mec1, and its phosphomimetic mutant S129E facilitates DNA repair[38,39]. Treatment of synchronized wild-type S-phase cells with hydroxyurea resulted in transient phosphorylation of H2A, being high after 30 min, but largely abolished after 60 min (ref. [40]) (Extended Data Fig. 2a). To eliminate possible contributions to the phosphorylation signal by Tel1, we repeated this experiment in *tel1Δ*, with comparable results (Fig. 2e). Remarkably, the *mec1-F2244L* mutant showed constitutive phosphorylation of H2A in all phases of the cell cycle. Treatment with the DNA-damaging agent 4-nitroquinoline *N*-oxide (4NQO) also resulted in robust phosphorylation of *MEC1* cells in G1 and G2 (Fig. 2e).

Constitutively active *mec1-F2244L* replaces the need for Mec1 checkpoint activators. A minimally active checkpoint is important for the viability of yeast. Cells that are *tel1Δ*, but wild-type for *MEC1*, show extreme growth defects and massive genome instability
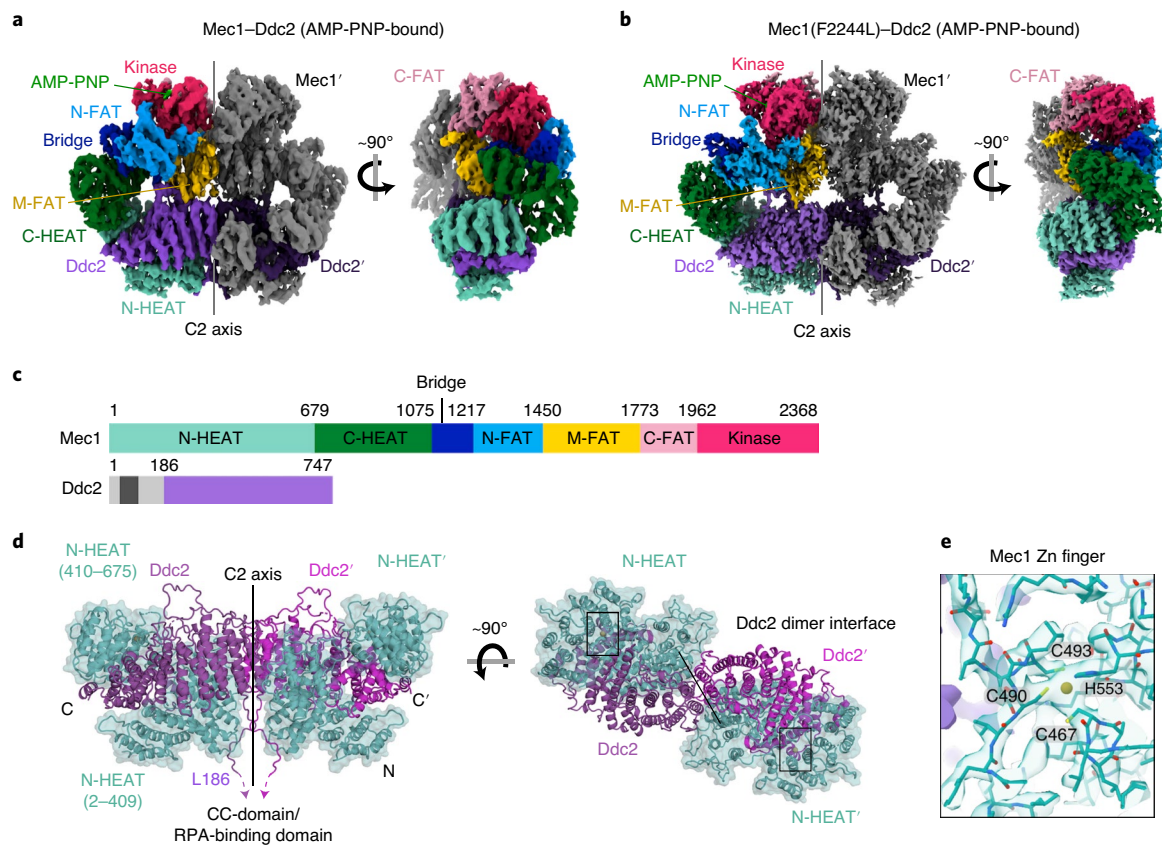
Fig. 3 | Overall cryo-EM structures of Mec1–Ddc2–AMP-PNP and the constitutively active Mec1(F2244L)–Ddc2–AMP-PNP complex.
a,b, Two orthogonal views of the Mec1–Ddc2 AMP-PNP-bound complex resolved to 3.8 Å (**a**), and two orthogonal views of the constitutively active Mec1(F2244L)–Ddc2–AMP-PNP complex resolved to 2.8-Å resolution (**b**). Structurally distinct domains are colored; red, kinase; pink, C-terminal-FAT; yellow, middle-FAT; blue, N-terminal-FAT; navy, bridge; green, C-terminal HEAT; teal, N-terminal HEAT. The Ddc2 subunit is colored purple, and the nucleotide is colored bright green. The 2-fold symmetry (C2) axis is shown. The second Mec1–Ddc2 heterodimer is shown in gray (Mec1′) and dark purple (Ddc2′). **c**, Primary structure of Mec1 and Ddc2 proteins showing structural domains and their boundaries. **d**, The Ddc2 dimer is cradled and makes extensive interactions with Mec1 N-terminal HEAT repeat (N-HEAT) domain. The N-HEAT domain can be divided into two major regions contributing to Ddc2 association (residue ranges are shown). The N-terminal ~170 amino acids, which include the coiled-coil domain and RPA-interacting motif in Ddc2, are not visible in our structure. Prime symbol (′) denotes the symmetry-related copy within the dimer. **e**, A metal-bound CCHC zinc finger within the Mec1 N-HEAT domain. Cryo-EM density of the zinc finger region is shown with a coordinated zinc ion.

when all three activation mechanisms for Mec1 are eliminated in strain *MEC1 tel1Δ ddc1Δ dna2-WY128,130AA* (ref. [8,41]). The double point mutations in *DNA2* eliminate its checkpoint activity without compromising its essential DNA replication and repair functions. *Mec1-F2244L* but not a second copy of wild-type *MEC1* restored robust growth of the activator-deficient mutant in a dominant manner (Fig. 2f and Extended Data Fig. 2b). This strain is also moderately resistant to DNA damage and replication stress (Fig. 2f).

Consistent with previous results[8], the activator-deficient strain is defective for phosphorylation of both H2A and Rad53 in response to damage or stress (Fig. 2g, lanes 1–4). On the other hand, damage-dependent phosphorylation of both targets is restored with *mec1-F2244L* (lanes 5–8). While a substantial amount of H2A phosphorylation is observed without DNA damage, it is enhanced by 4NQO treatment, indicating that localization of the constitutively active Mec1-F2244L to stalled forks or DNA repair intermediates enhances its activity. As shown before in Fig. 2e, full phosphorylation response of Rad53 requires DNA damage.

Overview of the structures of Mec1–Ddc2 and Mec1(F2244L)–Ddc2. Our data suggest that Mec1(F2244L) mimics the activated state, which rescues activator-defective cell growth and confers increased DNA repair functionality. To provide a molecular basis

for its constitutive activity, we determined the Mec1(F2244L)–Ddc2 structure to 2.8 Å and a wild-type structure to 3.8-Å resolution, both in the presence of Mg^{2+}-AMP-PNP to mimic precatalysis state (Fig. 3a,b, Table 1 and Extended Data Figs. 3–5). We also obtained a structure of wild type in an apo form at lower resolution (4.3 Å), and its features are broadly similar to that of the nucleotide-bound form at this resolution (Table 1 and Extended Data Figs. 3 and 4). The high-quality cryo-EM three-dimensional (3D) reconstruction of the Mec1(F2244L)–Ddc2 Mg^{2+}-AMP-PNP-bound complex allowed us to unambiguously assign and build an atomic model for the entire Mec1 protein (residues 2–2,368) and Ddc2 from residue 187 to the C terminus (residue 747) (Fig. 3a–d). We assign a series of regions in Mec1 that are structurally related to the previously assigned domains of PIKKs[21], denoted as N-HEAT, C-HEAT, Bridge, N-FAT, M-FAT, C-FAT and Kinase (Fig. 3a–c). This model was fitted, refined and rebuilt into electron density maps of wild-type proteins, which are of lower resolution possibly due to intrinsic flexibility (Extended Data Fig. 4). We also observe a CCHC-type zinc finger (residues C467, C490, C493, H553) within the Mec1 N-HEAT domain, which likely performs a structural role to stabilize the interaction with Ddc2 (Fig. 3e).

Our structural model of Ddc2 and Mec1 NTDs differs substantially from a previously determined structure[27] (Extended Data
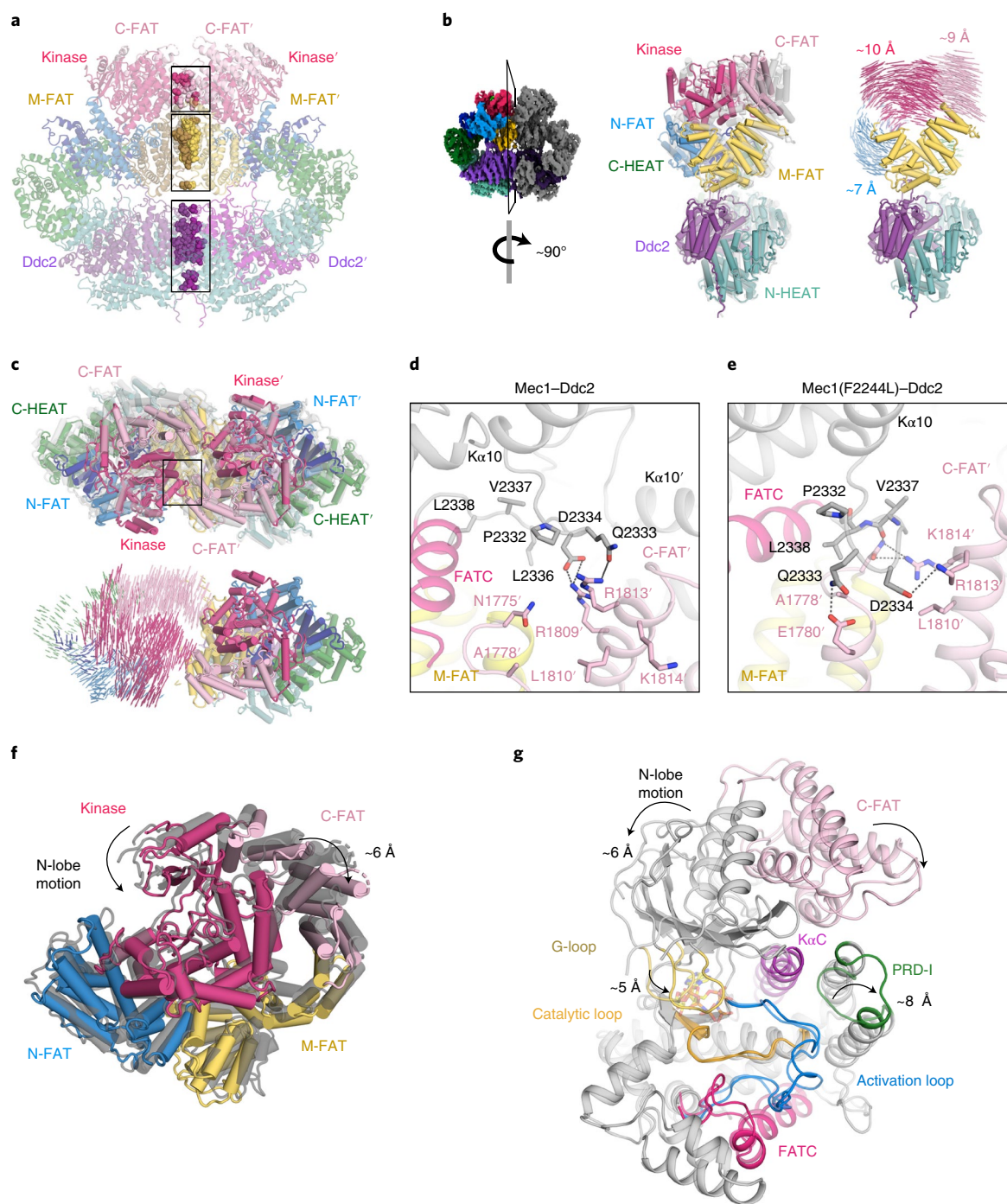
Fig. 4 | Global domain motions leading to Mec1 constitutive activity. a, Dimer interface highlighting three interacting layers; upper layer, formed by kinase and C-FAT domains (kinase–C-FAT′); middle layer, M-FAT–M-FAT′; lower layer, Ddc2–Ddc2′. Both Mec1–Ddc2 heterodimers are colored by domains as in Fig. 3a. **b**, Relative domain motion in the protomers between Mec1(F2244L)–Ddc2 and Mec1–Ddc2 (gray) when aligned on the adjacent symmetry-related protomer of the dimer. Vectors of the motion are shown, where the magnitude of the vector corresponds to the r.m.s. deviation difference for Cα atoms. M-FAT, Ddc2 and N-HEAT show minimal motion (less than 1Å). **c**, Same as in **b**, viewed down the dimer axis from the kinase domain showing the relative domain motion within the dimer when aligned on the right-hand-side protomer. **d,e**, Molecular details of the remodeled FATC-PRD loop that forms the kinase–C-FAT′ dimer interface in the wild-type structure (**d**) and in the F2244L structure (**e**). **f**, FAT and kinase domain (FAT–KIN) motion between Mec1(F2244L) and Mec1 (gray) structures when aligned on the C-lobe. **g**, Conformational changes in and around the active site between Mec1(F2244L) and Mec1 (gray) when aligned on the C-lobe. The FAT–KIN is colored by domain as in Fig. 3a, and the kinase domain is colored by catalytic feature as in Fig. 1b.

Figs. 6 and 7). In our model, Mec1 NTD is well-structured (Extended Data Fig. 6), forming a HEAT solenoid (termed N-HEAT) that cradles Ddc2 with a buried surface of nearly 7,000 Å² (Fig. 3d). This is consistent with earlier data showing that Ddc2 interacts with ~600

N-terminal residues of Mec1 (ref. [42]). In the previously published structural model, the first 200 amino acids of Mec1 were missing and instead this part was assigned as the Ddc2 NTD (Extended Data Figs. 6 and 7), in stark contrast to the crystal structure and biochemical
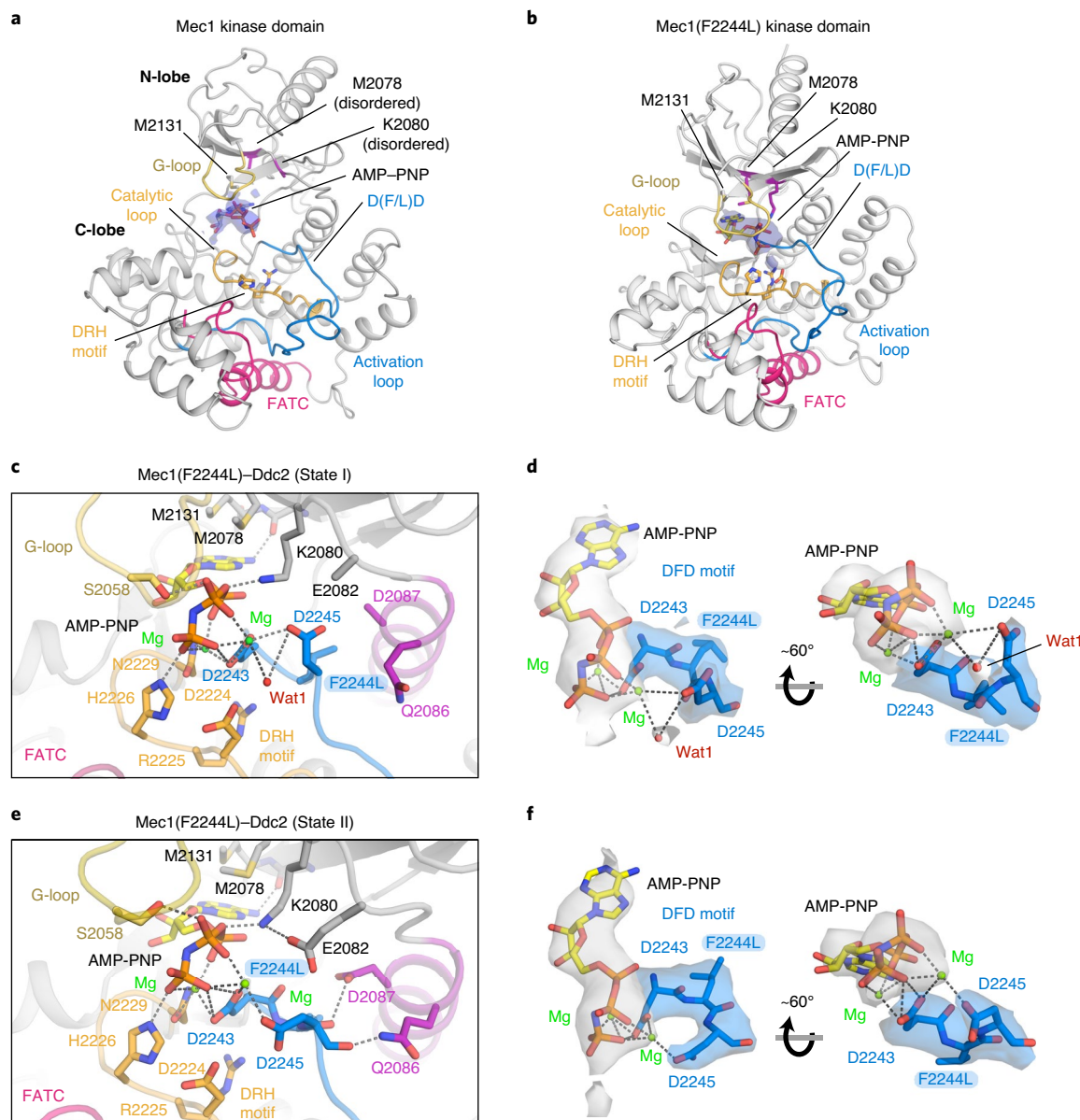
Fig. 5 | Magnesium-AMP-PNP binding configuration. a,b, Relative nucleotide-binding sites in the kinase domains of Mec1–Ddc2 (**a**) and the constitutively active Mec1(F2244L)–Ddc2 mutant (**b**). Cryo-EM electron density for AMP-PNP (blue) is shown, with locations of catalytically important features (colored and labeled as follows; catalytic loop, orange; activation loop, blue; G-loop, yellow; FATC, magenta) that are contributed by the N-lobe and C-lobe. N-lobe residues, M2078 and K2080, which are not visible in the Mec1–Ddc2 structure, are highlighted purple for clarity. The canonical kinase-specific HRD motif is actually DRH in PIKKs ([2224]DRH[2226] in Mec1). **c,** Molecular details of the Mec1(F2244L)–Ddc2 active-site cleft in one of the two subtly different states, denoted as State I. Nucleotide-coordinating residues are shown with hydrogen bonds (dashed lines). **d,** Two views of the cryo-EM density of the mutated D[F/L]D motif (F2244L) in State I (blue), along with electron density of AMP-PNP and Mg^{2+} (gray). The D[F/L]D (blue) and AMP-PNP (orange and yellow) are shown as sticks, while Mg^{2+} ions (green) and a coordinated water molecule (Wat1, red) are shown as spheres. **e,** The same as in **c** but for State II. **f,** The same as in **d** but for State II. Note the different side chain conformations of D2245 in **d** and **f**. The kinase features are colored as in panels **a** and **b**, except that the KαC is colored purple.

data showing that Ddc2 NTD possesses a coiled-coil domain, forming an elongated dimer, and an RPA-interacting domain[15,29]. Despite the use of full-length proteins, the Ddc2 NTD is missing in our 3D reconstruction, presumably due to these domains being flexibly tethered to the rest of Ddc2 by an ~50-amino acid linker. Our model thus reconciles and supports previous crystal structures, and models based on biochemical analysis. Our Ddc2 structural model shows that two of the Mec1-dependent phosphorylation sites of Ddc2 (T29, T40)[17] and the reported DNA-binding region (177–180) would be accessible[43].

Both wild-type and F2244L Mec1–Ddc2 form a dimer of heterodimers, as reported previously[13]. The dimer interface is composed of three layers; two are exclusively formed by the Mec1 dimer, with the kinase domain and C-FAT forming an upper layer, and M-FAT forming the middle layer. The lower layer is exclusively formed by the Ddc2 homodimer (Fig. 4a,b). Comparisons between the wild-type and F2244L structures show that dimer interfaces mediated by Ddc2 and M-FAT are largely unchanged, whereas the dimer interface formed by the kinase and C-FAT domain differ substantially (Fig. 4c–e). In the F2244L structure, an ~15° rotation
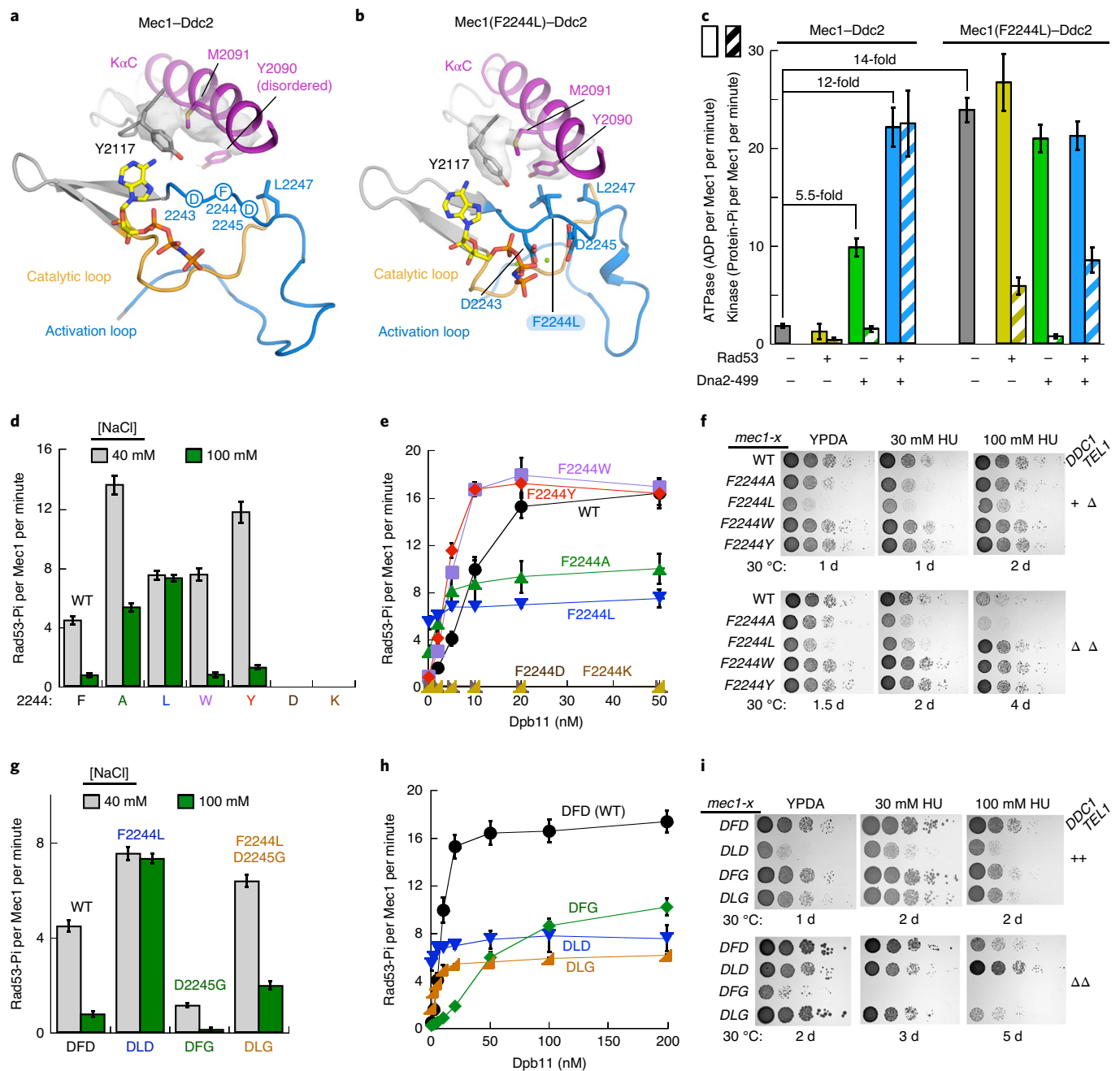
Fig. 6 | Structure–function analysis of the Mec1 activation DFD loop motif. a, Conformation of the activation loop (blue) and KαC (purple) in Mec1–Ddc2 showing the residues of the hydrophobic pocket (Y2090, M2091 and Y2117 with corresponding cryo-EM electron density). The exact side-chain conformation of the DFD motif is not known, and the residues are depicted by circles. AMP-PNP (yellow and orange) is shown as sticks. It should also be noted that the side chain of Y2090 is not visible, as demonstrated by a lack of density. **b**, In Mec1(F2244L)–Ddc2, the D[F/L]D motif is well ordered, along with the hydrophobic pocket, including Y2090, in which the F2244L side chain is buried. Also shown are AMP-PNP and Mg^{2+}. **c**, Comparative ATPase (solid bars) and kinase (striped bars) activities of Mec1–Ddc2 and Mec1(F2244L)–Ddc2 in the presence or absence of Rad53 and Dna2-499 (Methods). **d**, Basal activity of Mec1 mutants. F, A, L, W, Y, D and K refer to the amino acid substitutions of residue 2244. **e**, Dpb11 activation of Mec1 mutants. Half-maximal activation was observed at 10.3 ± 2.8 nM Dpb11 for wild-type Mec1, 4.3 ± 1.5 nM Dpb11 for Mec1(F2244W) and 3.2 ± 1.1 nM Dpb11 for Mec1(F2244Y). **f**, Growth of *MEC1* mutants, as described in the legend of Fig. 2. **g**, Basal activity of Mec1 mutants. **h**, Dpb11 activation of Mec1 mutants. Half-maximal activation was observed at 95 ± 25 nM Dpb11 for Mec1(D2245G). **i**, Growth of *MEC1* mutants, as described in the legend of Fig. 2. Error bars for panels **c**–**e**,**h** represent the mean $\pm$ s.e.m. of $n = 3$ independent assays. Data for graphs in panels **c**–**e**,**g**,**h** are reported as source data.

of the kinase domains around the *C*2 axis was observed, which shifts the kinase domains away from one another by up to 10 Å (Fig. 4b,c), altering the dimer interface (Fig. 4d,e). This displacement of the kinase domains is concomitant with a clockwise motion of the C-FAT relative to the kinase C-lobe (Fig. 4f) and kinase

N-lobe motion within a protomer (Fig. 4g and Supplementary Video 1). Further, the PRD-I in the F2244L mutant moves away from the nucleotide-binding pocket towards the dimer interface by up to 10 Å, retracting from the active site via a loop-to-helix transition (Fig. 4g). Overall, there are substantial conformational changes
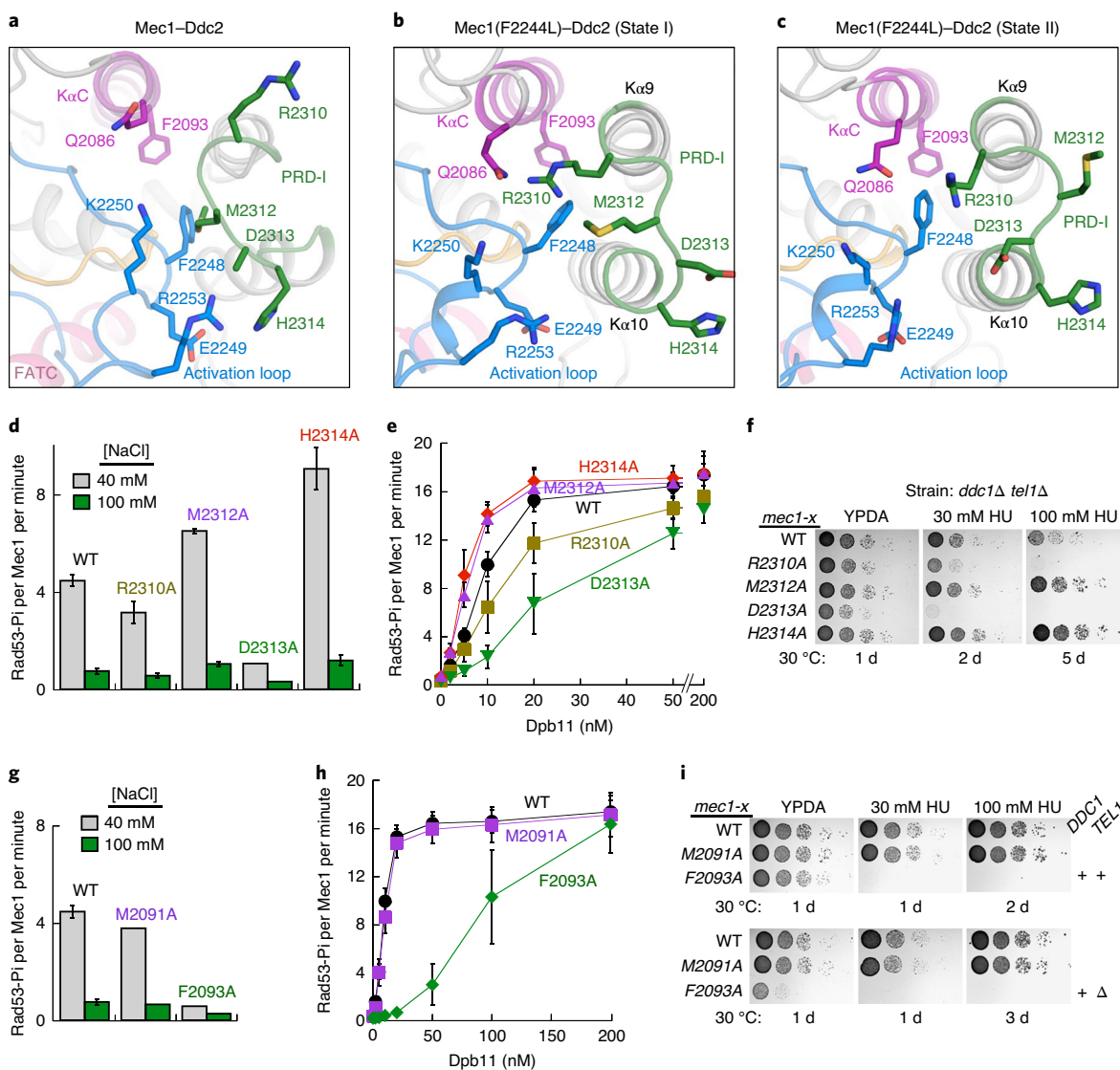
Fig. 7 | Structure–function analysis of the PRD-I loop and helix KαC (activation loop–interacting helix). a,b,c, Molecular details of the PRD-I and the activation loop comparing wild-type Mec1 kinase (**a**), constitutively active F2244L (State I) (**b**) and constitutively active F2244L (State II) (**c**). Active-site features are colored as in Fig. 5. **d**, Basal Mec1 activity. **e**, Dpb11 activation of Mec1. Half-maximal activation was observed at 10.3 ± 2.8 nM Dpb11 for wild-type Mec1, 15 ± 3.4 nM Dpb11 for Mec1(R2310A), 5.8 ± 1.5 nM Dpb11 for Mec1(M2312A), 36 ± 10 nM Dpb11 for Mec1(D2313A) and 5.16 ± 1.34 nM Dpb11 for Mec1(H2314A). **f**, Growth of *MEC1* mutants, as described in the legend of Fig. 2. **g**, Basal Mec1 activity. **h**, Dpb11 activation of Mec1. Half-maximal activity was observed at 11.53 ± 3.15 nM Dpb11 for Mec1(M2091A) and >100 nM Dpb11 for Mec1(F2093A). **i**, Growth of *MEC1* mutants, as described in the legend of Fig. 2. Error bars for panels **d,e,g,h** represent the mean $\pm$ s.e.m. of $n = 3$ independent assays. Data for graphs in panels **d,e,g,h** are reported as source data.

in and around the active site, domain movements within a protomer and changes at the dimer interface between the F2244L and wild-type proteins.

Conformational changes near the nucleotide-binding pocket reveal key regions for auto-inhibition and activation. In the wild-type structure, the triphosphate moiety of the bound nucleotide is too distant from the catalytic residues to allow robust activity (Fig. 5a). The catalytic loops in the wild-type and mutant structures remain largely unchanged (Figs. 4g and 5a,b). However, in the activated state, represented by Mec1(F2244L), the kinase N-lobe moves inwards, causing closure of the nucleotide-binding site (Figs. 4g and 5a,b and Supplementary Video 2). The nucleotide is moved ~2–3 Å towards the catalytic center and is now correctly presented to the DRH motif (mirrored HRD, Fig. 5a,b). Furthermore, the G-loop moves ~5 Å towards the nucleotide, enabling hydrogen

bonding of the invariant S2058 with the β–γ phosphates of AMP-PNP (Fig. 5c), as observed in mTOR[20]. In addition to the G-loop, the N-lobe contributes to nucleotide binding via hydrophobic interactions around the adenine ring, including M2078 (the so-called gatekeeper residue), and via an invariant K2080 hydrogen bonding with α–β phosphate (Fig. 5c).

Two highly similar conformations were obtained within the Mec1(F2244L) dataset, with one at 2.8 Å (State I) and the second at 3.2 Å (State II). Differences between these two activated states center around the D[F/L]D motif (Fig. 5c–f). While D2243, which coordinates both Mg²⁺ ions, remains largely unchanged, F2244L 'wobbles' in its hydrophobic pocket (Fig. 5c,e). Critically, D2245 coordinates the second Mg²⁺ in both states (Fig. 5c–f), suggesting a critical role for this motif in Mec1. However, the rotamer conformation of State II D2245 also allows E2082 to interact with the catalytically essential K2080 (Fig. 5e, equivalent to the E91:K72 salt bridge

in protein kinase A, a hallmark of an active state[44]). Additional contacts between the main chain of the D[F/L]D motif and side chains of D2087 and Q2086 are also observed (Fig. 5e). The extensive network of hydrogen bonds that stabilizes the activation loop suggests that State II might represent a more active configuration.

The noncanonical DFD motif of Mec1 plays a critical role in kinase activity. The remarkable properties of F2244 highlight its critical role in kinase activity and are corroborated by the structures (Fig. 6a,b). The differences in activity between wild type and Mec1(F2244L) could be manifold, for example, nucleotide binding, hydrolysis or phosphoryl transfer. We carried out a comparative ATPase analysis of wild type and Mec1(F2244L), in the presence or absence of Rad53 substrate and Dna2 activator (Fig. 6c). We performed identical assays with either α-^{32}P-ATP (total ADP formed) or γ-^{32}P-ATP (substrate phosphorylated) to determine whether ADP formation was productive (phosphate transfer to protein substrate) or unproductive (transfer to water). Wild-type Mec1 showed very low ATP turnover and kinase activity, unless Dna2 activator was present (Fig. 6c). Dna2 and Rad53 increased the ATPase 12-fold. Importantly, all ATP used is coupled to phosphoryl transfer to Rad53. However, in the absence of the Rad53, Dna2 caused an increase in unproductive hydrolysis. In contrast, the ATPase activity of Mec1(F2244L) alone is already ~14-fold higher than wild type. This is consistent with structural data showing that its nucleotide-binding site and all catalytic residues are properly assembled (Fig. 5c,e). With Rad53 substrate present, the increased ATP turnover is poorly coupled to kinase activity (Fig. 6c). This could be due to the altered environment of the mutant, which may still retain water in the active site for unproductive transfer[45]. Similar results were obtained with Dpb11 as activator, although the analysis was more complicated because Dpb11 is also an Mec1 substrate (Extended Data Fig. 8c).

We also carried out an ATP concentration-dependence kinase activity assay to determine binding affinity. The apparent ATP K_m for Mec1(F2244L) is ~5-fold lower than that for wild type in the absence of activators (Extended Data Fig. 8a,b), suggesting that the activated form, via activator binding or constitutive active mutant, promotes ATP binding. These results are consistent with the structures. In the wild-type protein without activator, the G-loop is further away from the catalytic center, resulting in an ATP binding pocket with lower affinity (Figs. 5a,b and 6a,b). These data indicate that the increased activity in F2244L is due to enhanced nucleotide binding and hydrolysis.

To understand why the F2244L mutation induces such dramatic changes, we examined the environment surrounding F2244. Mutant L2244 is inserted in a hydrophobic pocket formed by Y2117, Y2090 and M2091 of the KαC and L2247 of the activation loop (Fig. 6b). Disrupting these interactions by substituting F2244 with a charged residue (F2244K or F2244D) eliminated all kinase activity (Fig. 6d,e), and the mutants were unable to complement lethality of *mec1Δ* (Extended Data Fig. 8d). Mutation to the small hydrophobic Ala yielded a lower activity enzyme than F → L (Fig. 6d,e), probably due to increased flexibility of the activation loop. Given these considerations, a larger hydrophobic residue could stabilize the active state. Indeed, while at 100 mM NaCl the basal activities of both Mec1(F2244W) and Mec1(F2244Y) were similar to wild type, the mutants showed increased apparent affinity for Dpb11 and higher stimulated activity (Fig. 6e). Furthermore, while the aromatic substitutions are phenotypically silent in a wild-type (not shown) or *tel1Δ* strain, they showed an increased resistance to hydroxyurea in the checkpoint-compromised *tel1Δ ddc1Δ* strain (Fig. 6f).

While both the F2244L and the F2244W/Y mutants show hyperactivity, they are mechanistically distinct. Mec1 activation requires relief of the inhibition state and establishment of the active site. In the simplest interpretation of this model, Mec1 is in a two-state

equilibrium between the inhibited and activated states, which is normally regulated by Dpb11 (or another activator). The F2244W/Y mutants have low basal activity similar to wild type (Fig. 6d), suggesting that they are largely in the inhibited state without activator, but they have a lower energy barrier for Dpb11-mediated transition to the activated state. Therefore, these mutants are phenotypically silent in a checkpoint-proficient strain. In contrast, for F2244L, the equilibrium between the inhibited and activated states is strongly shifted to that of the activated state in the absence of activator, and hence the growth defect of *mec1-F2244L* in a checkpoint-proficient strain due to elevated Mec1 activity. On the other hand, in checkpoint-compromised *tel1Δ ddc1Δ*, the F2244L mutant shows increased resistance to hydroxyurea because of its constitutive activity, whereas the F2244W/Y mutants show increased resistance because a lower level of activator suffices for a robust response.

Changing the DFD motif to DFG, the canonical motif for most protein kinases, highlights the importance of the Mg^{2+} chelation function of Mec1 D2245. Mec1(D2245G) showed a large decrease in the apparent affinity for Dpb11, and a decreased basal activity (Fig. 6g,h). The mutant showed strong defects when tested in a checkpoint-compromised background (*tel1Δ ddc1Δ*) (Fig. 6i). When the central motif was mutated to DLG, the motif found in Tel1^{ATM}, a robust response to Dpb11 was restored (Fig. 6h), and the double mutant showed no phenotype (Fig. 6i), suggesting that the defects caused by D2245G are rescued by F2244L. Remarkably, among the variations in this motif observed in 640 Mec1^{ATR} species, there is not a single occurrence of the DLD motif, which causes constitutive activity (Extended Data Fig. 1d). Mutations in this motif are also not found in the cancer mutation databases.

The Mec1 PRD-I prohibits an active conformation of the activation loop. The PRD-I is a poorly conserved element between Kα9 and Kα10, and has a length range of 6–9 amino acids in Mec1^{ATR}, 43–50 in Tel1^{ATM} and >70 residues in mTOR (ref. [46]). In Tel1^{ATM}, PRD-I coincides with the putative substrate binding site, acting as an auto-inhibitory element[21]. While substrate competition is a clear role for the PRD-I in Tel1^{ATM} and other PIKKs, the PRD-I in Mec1 is only a short connecting linker (^{2309}DRNMDHSIQ^{2317}).

Wild-type Mec1 does not adopt a defined DFD conformation (Fig. 6a and Extended Data Fig. 9a–c). This is consistent with the wide range of DFG configurations that render kinases inactive but limited conformations that enable activity[44,46,47]. Nevertheless, our structural data suggest a hydrophobic network between PRD-I and the activation loop in the inactive state (Fig. 7a). In the activated state, PRD-I moves away from the activation loop and undergoes a loop-to-helix transition, shortening the loop between Kα9 and Kα10 (Figs. 4g and 7a–c and Supplementary Video 3). The retraction of PRD-I from the activation loop upon activation suggests that PRD-I may also play an auto-inhibitory function in Mec1. To further understand the role of PRD-I, we mutated several residues (Fig. 7d–f). In the wild-type structure, M2312 sits above the highly conserved F2248, similar to W2701 in the Tel1 PRD-I (Fig. 7a and Extended Data Fig. 9d,e). D2313 and H2314 form putative interactions with R2253 and E2249 of the activation loop. M2312A and H2314A mutations, which likely perturb PRD-I/activation loop interactions, indeed showed modestly increased basal- and Dpb11-stimulated activity (Fig. 7d,e). D2313 may stabilize the activated states. In State I, it interacts with H2314 in the newly formed helix, suggesting that it could aid the loop-to-helix transition of the PRD-I (Fig. 7b). In State II, D2313 moves inwards, coinciding and possibly assisting with M2312 flipping out (Fig. 7c). Remarkably, the D2313A mutation showed strongly reduced basal and activated kinase activity (Fig. 7d,e), suggesting an important role in PRD-I re-arrangement during activation. Even though R2310 undergoes a large rotation upon activation (Fig. 7b), the R2310A mutation, showing slightly reduced activity, was less informative. The differ-

ences in biochemical activity of these PRD-I mutants are reflected in their phenotypes in yeast. In the checkpoint-compromised strain (*tel1Δ ddc1Δ*), the *mec1-M2312A* and *mec1-H2314A* mutants with increased biochemical activity were more resistant to hydroxyurea than wild type (Fig. 7f). An explanation for the increased resistance is the same as proposed above for the F2244W/Y mutants.

A pocket in the activation loop–interacting helix KαC docks F2244 in the active state. The motion of the KαC, which directly contacts the activation loop and the PRD, may couple the activation loop conformation with the release of the PRD-I. M2091 and F2093 are highly conserved residues in this network. Alanine mutation of M2091, which forms part of the hydrophobic pocket in which F2244 is predicted to sit when activated (Fig. 6a,b), behaved similarly to wild type (Fig. 7g–i). This mutation may be tolerated because Y2117 and Y2090 are still able to wedge F2244 in its correct position. On the other hand, mutation of F2093, which is sandwiched between L2299 of Kα9 (PRD) and L2220, adjacent to the catalytic loop, showed low basal kinase activity and a strong defect in activation by Dpb11 (Fig. 7g,h). Comparison between the activated and inactive structures shows that the F2093A mutation would disturb the packing of the Kα9 and KαC such that it may become more difficult to fully activate, thereby explaining the Dpb11-mediated stimulation defects (Fig. 7a–c), and compromised growth in a *tel1Δ* mutant and extreme hydroxyurea sensitivity (Fig. 7i).

Discussion

In this work, we present an integrated analysis of key functional regions in Mec1[ATR] to unravel the complex regulatory network that governs its low basal activity and activation, and the requirement of kinase activity and activators in normal growth and response to damage or replication stress. Constitutive activity of Mec1(F2244L) was marked by poor yeast growth, likely by increased phosphorylation of cell-cycle targets. We detected high, constitutive phosphorylation of histone H2A (the yeast form of γ-H2AX), a hallmark of DNA repair (Fig. 2e)[38,39]. When the checkpoint circuitry is compromised because of Mec1 activator loss, 9-1-1, Dpb11 and Dna2 (Fig. 2f,g), the constitutive mutant rescues the growth phenotype, indicating that there is an optimal window of Mec1 activity for cell-cycle progression and growth.

A two-pronged activation mechanism reverses inhibition by PRD-I and reconfigures the activation loop. Our data indicate that the PRD-I is a key regulatory element, by holding the activation loop in an inactive conformation through a network of weakly held interactions. The inhibition can be released through mutagenesis or by activator binding, resulting in stimulation of basal kinase activity. F2244 is critical for both the auto-inhibited and activated states, reminiscent of the DFG-in/out activation mechanism in many kinases[47,48]. Altered basal and stimulated activity are observed when the DFD Phe is substituted for either larger (Trp or Tyr) or smaller (Leu or Ala) hydrophobic residues. Interestingly, Mnks (MAP kinase-interacting kinases) also possess a noncanonical DFD motif with the Phe placed in an auto-inhibited conformation in the absence of activators[49].

Our studies suggest that Mec1 activation requires (1) the removal of the inhibition imposed by PRD-I and (2) the establishment of the activated state. The two requirements are interconnected with the relocation of PRD-I coupled to conformational changes in C-FAT and N-lobe, which contribute to the active-site reconfiguration. This two-pronged mechanism is reflected in the highly complex behavior of many of the mutants, as many regions, for example, the activation loop and PRD-I, are involved in both maintaining auto-inhibition and establishing activation. Within PIKKs, a C-FAT rotation and N-lobe closure were also proposed for DNA-PKcs, mTORC1 and ATM[Tel1], via allosteric conformational changes upon

activator binding, which is remote from the kinase domain[22–24,50,51]. It thus seems that C-FAT rotation and N-lobe movement may be conserved features in all PIKKs irrespective of the activator binding site or exact activation mode. Mec1 employs an activation mechanism that contains elements operating in mTORC1 (FAT and N-lobe movement), and kinases using a DFG-in/out mechanism. Whether these features are shared by other PIKKs remains to be determined.

The unique DFD/N in Mec1[ATR] is associated with its distinctive activation mechanism. The unique activation mechanism we unraveled here centers around the DFD motif. Indeed, although the majority of PIKKs possess a canonical DFG motif, mutating the DFD motif to DFG resulted in an incapacitated kinase. Our structures suggest that this is due to differences in Mg^{2+} coordination. Unlike in other PIKKs, in Mec1, second Mg^{2+} coordination is stabilized by the second aspartate of its DFD motif (Fig. 5c–f and Extended Data Fig. 9f–i), and likely also by the asparagine of the more common DFN motif, and this does not require substrate binding. This is indeed consistent with the observation that the activated form of wild-type Mec1 can hydrolyze ATP in the absence of substrate, and the F2244L mutant can achieve maximum ATPase activity without substrate or activator (Fig. 6c). In many other kinases, second Mg^{2+} coordination involves substrate binding. In some kinases, such as CDK2 and PKA, the second Mg^{2+} binding is shown to be the final, rate-limiting step in catalysis[45,52]. The differences in second Mg^{2+} coordination might thus reflect differences in the rate-limiting step among PIKKs, be it substrate binding or establishing the active site, as observed for Mec1.

Online content

Any methods, additional references, Nature Research reporting summaries, source data, extended data, supplementary information, acknowledgements, peer review information; details of author contributions and competing interests; and statements of data and code availability are available at https://doi.org/10.1038/s41594-020-00522-0.

References

1. Weber, A. M. & Ryan, A. J. ATM and ATR as therapeutic targets in cancer. *Pharmacol. Ther.* **149**, 124–138 (2015).
2. Lovejoy, C. A. & Cortez, D. Common mechanisms of PIKK regulation. *DNA Repair (Amst.)* **8**, 1004–1008 (2009).
3. Kumagai, A., Lee, J., Yoo, H. Y. & Dunphy, W. G. TopBP1 activates the ATR-ATRIP complex. *Cell* **124**, 943–955 (2006).
4. Mordes, D. A., Nam, E. A. & Cortez, D. Dpb11 activates the Mec1–Ddc2 complex. *Proc. Natl Acad. Sci. USA* **105**, 18730–18734 (2008).
5. Mordes, D. A., Glick, G. G., Zhao, R. & Cortez, D. TopBP1 activates ATR through ATRIP and a PIKK regulatory domain. *Genes Dev.* **22**, 1478–1489 (2008).
6. Navadgi-Patil, V. M. & Burgers, P. M. Yeast DNA replication protein Dpb11 activates the Mec1/ATR checkpoint kinase. *J. Biol. Chem.* **283**, 35853–35859 (2008).
7. Navadgi-Patil, V. M. & Burgers, P. M. The unstructured C-terminal tail of the 9-1-1 clamp subunit Ddc1 activates Mec1/ATR via two distinct mechanisms. *Mol. Cell* **36**, 743–753 (2009).
8. Kumar, S. & Burgers, P. M. Lagging strand maturation factor Dna2 is a component of the replication checkpoint initiation machinery. *Genes Dev.* **27**, 313–321 (2013).
9. Paull, T. T. Mechanisms of ATM activation. *Annu. Rev. Biochem.* **84**, 711–738 (2015).
10. Hailemariam, S., Kumar, S. & Burgers, P. M. Activation of Tel1[ATM] kinase requires Rad50 ATPase and long nucleosome-free DNA but no DNA ends. *J. Biol. Chem.* **294**, 10120–10130 (2019).
11. Wanrooij, P. H., Tannous, E., Kumar, S., Navadgi-Patil, V. M. & Burgers, P. M. Probing the Mec1ATR checkpoint activation mechanism with small peptides. *J. Biol. Chem.* **291**, 393–401 (2016).

12. Thada, V. & Cortez, D. Common motifs in ETAA1 and TOPBP1 required for ATR kinase activation. *J. Biol. Chem.* **294**, 8395–8402 (2019).

13. Sawicka, M. et al. The dimeric architecture of checkpoint kinases Mec1ATR and Tel1ATM reveal a common structural organization. *J. Biol. Chem.* **291**, 13436–13447 (2016).

14. Ball, H. L. & Cortez, D. ATRIP oligomerization is required for ATR-dependent checkpoint signaling. *J. Biol. Chem.* **280**, 31390–31396 (2005).

15. Deshpande, I. et al. Structural Basis of Mec1-Ddc2-RPA Assembly and Activation on Single-Stranded DNA at Sites of Damage. *Mol. Cell* **68**, 431–445.e5 (2017).

16. Zou, L. & Elledge, S. J. Sensing DNA damage through ATRIP recognition of RPA-ssDNA complexes. *Science* **300**, 1542–1548 (2003).

17. Memisoglu, G. et al. Mec1ATR autophosphorylation and Ddc2ATRIP phosphorylation regulates DNA damage checkpoint signaling. *Cell Rep.* **28**, 1090–1102.e3 (2019).

18. Adams, J. A. Kinetic and catalytic mechanisms of protein kinases. *Chem. Rev.* **101**, 2271–2290 (2001).

19. Lempiainen, H. & Halazonetis, T. D. Emerging common themes in regulation of PIKKs and PI3Ks. *EMBO J.* **28**, 3067–3073 (2009).

20. Yang, H. et al. mTOR kinase structure, mechanism and regulation. *Nature* **497**, 217–223 (2013).

21. Yates, L. A. et al. Cryo-EM structure of nucleotide-bound Tel1ATM unravels the molecular basis of inhibition and structural rationale for disease-associated mutations. *Structure* **28**, 96–104.e3 (2020).

22. Sibanda, B. L., Chirgadze, D. Y., Ascher, D. B. & Blundell, T. L. DNA-PKcs structure suggests an allosteric mechanism modulating DNA double-strand break repair. *Science* **355**, 520–524 (2017).

23. Gat, Y. et al. InsP6 binding to PIKK kinases revealed by the cryo-EM structure of an SMG1–SMG8–SMG9 complex. *Nat. Struct. Mol. Biol.* **26**, 1089–1093 (2019).

24. Jansma, M. et al. Near-complete structure and model of Tel1ATM from *Chaetomium thermophilum* reveals a robust autoinhibited ATP state. *Structure* **28**, 83–95.e5 (2020).

25. Mallory, J. C. & Petes, T. D. Protein kinase activity of Tel1p and Mec1p, two *Saccharomyces cerevisiae* proteins related to the human ATM protein kinase. *Proc. Natl Acad. Sci. USA* **97**, 13749–13754 (2000).

26. Paciotti, V., Clerici, M., Scotti, M., Lucchini, G. & Longhese, M. P. Characterization of *mec1* kinase-deficient mutants and of new hypomorphic *mec1* alleles impairing subsets of the DNA damage response pathway. *Mol. Cell. Biol.* **21**, 3913–3925 (2001).

27. Wang, X. et al. 3.9 Å structure of the yeast Mec1-Ddc2 complex, a homolog of human ATR-ATRIP. *Science* **358**, 1206–1209 (2017).

28. Rao, Q. et al. Cryo-EM structure of human ATR-ATRIP complex. *Cell Res.* **28**, 143–156 (2018).

29. Ball, H. L. et al. Function of a conserved checkpoint recruitment domain in ATRIP proteins. *Mol. Cell. Biol.* **27**, 3367–3377 (2007).

30. Gangadhara, G. et al. A class of highly selective inhibitors bind to an active state of PI3Kγ. *Nat. Chem. Biol.* **15**, 348–357 (2019).

31. Wanrooij, P. H. & Burgers, P. M. Yet another job for Dna2: checkpoint activation. *DNA Repair (Amst.)* **32**, 17–23 (2015).

32. Jacobsen, D. M., Bao, Z. Q., O'Brien, P., Brooks, C. L. III. & Young, M. A. Price to be paid for two-metal catalysis: magnesium ions that accelerate chemistry unavoidably limit product release from a protein kinase. *J. Am. Chem. Soc.* **134**, 15357–15370 (2012).

33. Burtelow, M. A., Roos-Mattjus, P. M., Rauen, M., Babendure, J. R. & Karnitz, L. M. Reconstitution and molecular analysis of the hRad9-hHus1-hRad1 (9-1-1) DNA damage responsive checkpoint complex. *J. Biol. Chem.* **276**, 25903–25909 (2001).

34. Majka, J. & Burgers, P. M. Yeast Rad17/Mec3/Ddc1: a sliding clamp for the DNA damage checkpoint. *Proc. Natl Acad. Sci. USA* **100**, 2249–2254 (2003).

35. Allen, J. B., Zhou, Z., Siede, W., Friedberg, E. C. & Elledge, S. J. The SAD1/RAD53 protein kinase controls multiple checkpoints and DNA damage-induced transcription in yeast. *Genes Dev.* **8**, 2401–2415 (1994).

36. Sanchez, Y. et al. Regulation of RAD53 by the ATM-like kinases MEC1 and TEL1 in yeast cell cycle checkpoint pathways. *Science* **271**, 357–360 (1996).

37. Ma, J. L., Lee, S. J., Duong, J. K. & Stern, D. F. Activation of the checkpoint kinase Rad53 by the phosphatidyl inositol kinase-like kinase Mec1. *J. Biol. Chem.* **281**, 3954–3963 (2006).

38. Downs, J. A., Lowndes, N. F. & Jackson, S. P. A role for *Saccharomyces cerevisiae* histone H2A in DNA repair. *Nature* **408**, 1001–1004 (2000).

39. Fink, M., Imholz, D. & Thoma, F. Contribution of the serine 129 of histone H2A to chromatin structure. *Mol. Cell. Biol.* **27**, 3589–3600 (2007).

40. Puddu, F., Piergiovanni, G., Plevani, P. & Muzi-Falconi, M. Sensing of replication stress and Mec1 activation act through two independent pathways involving the 9-1-1 complex and DNA polymerase ε. *PLoS Genet.* **7**, e1002022 (2011).

41. Lanz, M. C. et al. Separable roles for Mec1/ATR in genome maintenance, DNA replication, and checkpoint signaling. *Genes Dev.* **32**, 822–835 (2018).

42. Bandhu, A., Kang, J., Fukunaga, K., Goto, G. & Sugimoto, K. Ddc2 mediates Mec1 activation through a Ddc1- or Dpb11-independent mechanism. *PLoS Genet.* **10**, e1004136 (2014).

43. Rouse, J. & Jackson, S. P. Lcd1p recruits Mec1p to DNA lesions in vitro and in vivo. *Mol. Cell* **9**, 857–869 (2002).

44. Huse, M. & Kuriyan, J. The conformational plasticity of protein kinases. *Cell* **109**, 275–282 (2002).

45. Bao, Z. Q., Jacobsen, D. M. & Young, M. A. Briefly bound to activate: transient binding of a second catalytic magnesium activates the structure and dynamics of CDK2 kinase for catalysis. *Structure* **19**, 675–690 (2011).

46. Williams, R. M., Yates, L. A. & Zhang, X. Structures and regulations of ATM and ATR, master kinases in genome integrity. *Curr. Opin. Struct. Biol.* **61**, 98–105 (2020).

47. Ung, P. M. & Schlessinger, A. DFGmodel: predicting protein kinase structures in inactive states for structure-based discovery of type-II inhibitors. *ACS Chem. Biol.* **10**, 269–278 (2015).

48. Modi, V. & Dunbrack, R. L. Jr. Defining a new nomenclature for the structures of active and inactive kinases. *Proc. Natl Acad. Sci. USA* **116**, 6818–6827 (2019).

49. Jauch, R. et al. Mitogen-activated protein kinases interacting kinases are autoinhibited by a reprogrammed activation segment. *EMBO J.* **25**, 4020–4032 (2006).

50. Yang, H. et al. Mechanisms of mTORC1 activation by RHEB and inhibition by PRAS40. *Nature* **552**, 368–373 (2017).

51. Yin, X., Liu, M., Tian, Y., Wang, J. & Xu, Y. Cryo-EM structure of human DNA-PK holoenzyme. *Cell Res.* **27**, 1341–1350 (2017).

52. Bastidas, A. C. et al. Phosphoryl transfer by protein kinase A is captured in a crystal lattice. *J. Am. Chem. Soc.* **135**, 4788–4798 (2013).

Methods

Yeast strains, plasmids and proteins. Yeast strains used in this study were prepared using PCR-based methods for gene disruption in which marker cassettes flanked by 100–200 base pairs of regions homologous to the targeted gene were synthesized and used to transform C10-2A strain (W303 *RAD5*)[53] for genomic integration. *S. cerevisiae MEC1* is an essential gene; however, the lethality of *mec1Δ* mutants is rescued by deletion of the ribonucleotide reductase inhibitor *SML1* (refs. [54,55]). In our genetic analysis, we have used strains that are *SML1* wild type. PY405 (MATa *ade2-1 can1-100 his3-11,15 leu2-3,112 trp1-1 ura3-1 mec1Δ::KanMX* containing pGM004 (*MEC1 URA3*)) was derived from C10-2A. Integration of *tel1Δ::NAT* in PY405 yielded PY406, and further integration of *ddc1Δ::HIS3* yielded strain PY414. The complementing plasmid pGM004 contains the *MEC1* gene on a centromeric plasmid under control of its own promoter, with *URA3* as both selectable and counterselectable (on 5-fluoroorotic acid) marker[17]. Transformants were selected on yeast peptone dextrose (YPD) plates containing the respective drug and verified by PCR analysis.

PY270 (MATa *can1 his3-Δ200 leu2 trp1 ura3-52 dna2Δ::HIS3 ddc1Δ::KanMX4 tel1Δ::NAT pBL583 (MEC1 URA3)*) was described previously[8]. For each of the Mec1 mutants, we generated a centromere plasmid: p(*mec1-x LEU2*) is pBL905-x (*mec1-x ARS1 CEN4 LEU2*) for genetic analysis[26]. A 2-μm plasmid, pBL904-x (2-μm ori *TRP1 mec1-x DDC2*), with the *mec1-x* and *DDC2* genes placed under control of the galactose-inducible *GAL1-10* promoter, was used for overproduction of the Mec1–Ddc2 complex[13]. *MEC1* mutants were made using standard methodology and all mutants were verified by DNA sequencing. Other plasmids have been described previously[8]. Purification of Dpb11 and Dna2(1–499) was as described[8].

Purification of Mec1 mutants. Strain PY252 (MATα *can1 his3 leu2 trp1 ura3 GAL pep4Δ::HIS3 nam7Δ::KANMX4 mec1Δ::KANMX6 sml1Δ::HYG*) was used to overexpress Mec1 or Mec1 mutants from the plasmid pBL904-x series, essentially as described[13], with some modifications. After galactose induction of 12 l of growth culture, cells were collected, lysed and subjected to affinity purification on IgG beads (2 ml). After extensive washing steps, the protein was eluted from the column by overnight incubation with HRV-3C protease at 4 °C. After elution, the Mec1 preparations were stabilized with 1 M final trimethylamine *N*-oxide before freezing and storage.

Mec1 kinase assay. Throughout this study, we used the kinase-dead version (K227A) of Rad53, fused to the glutathione-*S*-transferase (GST) purification tag (GST-Rad53-kd), as substrate for Mec1 kinase. Phosphorylation of 600 nM Rad53, or as indicated, was performed in a 10-μl assay containing 25 mM HEPES-NaOH pH 7.4, 2% glycerol, 1 mM DTT, 20 μg ml⁻¹ BSA, 0.08% ampholytes pH 3.5–10, 8 mM Mg-acetate, 100 μM ATP, 0.5 μCi [γ-³²P] ATP or as indicated, 40 or 100 mM NaCl final concentration (including contributions made by protein storage buffers) and 3 nM Mec1. Reactions were initiated by adding the indicated concentrations of Dpb11, Dna2-499 or Dna2-1 peptide[8], and incubated at 30 °C for 10 min. Reactions were quenched by adding 5 μl of 2.5× SDS–PAGE loading dye and heated at 95 °C. Samples were separated on 8% SDS–PAGE gel, dried and exposed to phosphor screen (GE healthcare), and imaged with a phosphoimager. The bands were quantified using ImageQuant and plotted using KaleidaGraph. The activity of the Mec1 mutants was evaluated with respect to wild-type Mec1, overexpressed and purified analogously. Most assays were carried out in triplicate and the error bars in the figures represent the standard error of the mean. Assays with mutants with low or no activity were carried out in duplicate and the plots show the average without error bars.

Mec1 ATPase. The assay was carried out essentially as described above in assay buffer with 100 mM NaCl and 100 μM [α-³²P], and 200 nM Dna2-499 and 600 nM GST-Rad53-kd, where indicated. The concentration of Mec1 or Mec1-F2244L was raised to 10 nM to achieve higher formation of ADP. Aliquots were processed and the data quantified essentially as described[56]. A maximum of 15% ATP hydrolysis was observed. For the experiment in Fig. 6c and Extended Data Fig. 8c, this experiment was matched exactly with a substitution of [α-³²P] by [γ-³²P] ATP, and protein phosphorylation (Rad53 plus Dna2-499 or Dpb11) quantified.

Yeast cell growth and analysis. Standard media were used for yeast cell growth. Yeast strains PY405, PY406 and PY414 were transformed with plasmid pBL905 or its derivatives and selected on synthetic complete selection media, SC-Ura-Leu plates. Transformants were grown overnight in SC-Leu medium, and plated on SC-Leu plates containing 5-fluoroorotic acid to allow growth only of cells that had lost plasmid pGM004 (*URA3 MEC1*). These strains were grown overnight in SC-Leu medium and tenfold serial dilutions were spotted onto YPD plates, with or without hydroxyurea, as indicated. Plates were incubated at 30 °C for varying times and photographed.

Yeast cell synchronization and FACS analysis were essentially carried out as described[57]. First, 200 mM hydroxyurea or 2 μg ml⁻¹ 4NQO (4-nitroquinoline *N*-oxide) was added as indicated in the figures. For western analysis, the antibodies used were anti-Rad53 (ab104232; RRID:AB_2687603) and anti-histone H2A (phospho S129, ab15083; RRID:AB_301630), both from Abcam, at

1:2,000 and 1:500 dilution, respectively. The Rad53 antibody recognizes both unphosphorylated and phospho-Rad53, whereas the ab15083 antibody only recognizes phospho-H2A. Rad53 blots were developed using anti-rabbit IgG-alkaline phosphatase conjugated secondary antibody (Sigma A3687) at 1:10,000 dilution and imaged using a Typhoon phosphoimager in the fluorescence mode. H2A blots were developed using anti-rabbit IgG HRP-linked secondary antibody (Cell Signaling 7074S) at 1:2,000 dilution in 5% fat-free milk prepared in Tris-buffered saline with Tween (TBST) and analyzed using a Thermo Scientific myECL imager.

Electron microscopy grid preparation. A frozen aliquot of purified *Saccharomyces cerevisiae* Mec1^WT–Ddc2 or Mec1(F2244L)–Ddc2 was diluted using sequential addition of 10-μl volumes of buffer (50 mM Tris-HCl, 50 mM NaCl, pH 7.4, supplemented with AMP-PNP and magnesium acetate), and was incubated for 30 min on ice. The final concentrations of samples were as follows: Mec1–Ddc2 (apo), ~100 nM; Mec1–Ddc2:AMP-PNP, ~100 nM, 5 mM AMP-PNP, 10 mM Mg(OAc)₂; and Mec1(F2244L)–Ddc2:AMP-PNP, ~80 nM, 2 mM AMP-PNP, 5 mM Mg(OAc)₂. Approximately 4 μl of the sample was deposited onto Lacey Carbon 300 mesh gold grids that also have an additional ultrathin carbon support layer (Ted Pella), which were plasma-cleaned for 20–30 s in air before sample application. Samples were vitrified by plunge freezing in liquid ethane at liquid nitrogen temperature using a Vitrobot Mk IV (FEI) set with a blotting force of −6, a waiting time of 60 s and a blotting time of 2 s, at 4 °C and 95% humidity.

Cryo-EM data acquisition. High-resolution movies were collected for Mec1–Ddc2 (apo), Mec1–Ddc2:AMP-PNP and Mec1(F2244L)–Ddc2 on a Titan KRIOS (Thermo Fisher), at either the Francis Crick Institute (London, UK) or eBIC, Diamond Light Source (Oxfordshire, UK). For all datasets, the microscopes were operated at 300 kV with the specimen at cryogenic temperatures (approximately −180 °C), with images recorded at 1–3-μm underfocus. Data for Mec1–Ddc2 (apo) were acquired on a Falcon III direct electron detector in linear mode at a nominal magnification of 75,000, corresponding to a pixel size of 1.09 Å, and a cumulative total electron dose of 59 e⁻ Å⁻². It was also necessary to collect a large fraction of the data using a stage tilt of −30°. A total of 15,097 micrographs (9,214 tilted and 5,833 untilted), fractionated into 11 frames, were collected. Data for Mec1–Ddc2–AMP-PNP and Mec1(F2244L)–Ddc2–AMP-PNP were acquired on a K3 direct electron detector (Gatan) with energy filter in super-resolution mode at a nominal magnification of 81,000, corresponding to a calibrated pixel size of 1.06 Å (super-resolution pixel size of 0.53 Å). For the Mec1–Ddc2–AMP-PNP grid, a total of 20,185 micrographs were collected, fractionated into 40 frames and with a cumulative total electron dose of ~43.6 e⁻ Å⁻². In the case of the Mec1(F2244L)–Ddc2–AMP-PNP mutant dataset, 15,902 micrographs with a cumulative electron dose of 51 e⁻ Å⁻² were collected and fractionated into 50 frames.

Cryo-EM image processing apo dataset. Movie frames were aligned, corrected for drift and beam-induced motion, and dose-weighted using MotionCor2 (ref. [58]) implemented in RELION-3.0 (ref. [59]). To estimate the contrast transfer function (CTF) gradient across a tilted micrograph, local CTF fitting was performed using Gctf[60]. Particles were picked with Gautomatch using re-projections of a low-resolution Mec1–Ddc2 EM structure[13,14] filtered to 30 Å. Particles were extracted in RELION-3.0 using a box size of 380 × 380 pixels and binned four times for initial processing. Due to the preferential orientation, specific views were low in number, and therefore to keep these two-dimensional (2D) classification was omitted as a first step. Instead, 3D classification was performed with an initial Mec1–Ddc2 model[13,14], filtered to 60 Å. Initial 3D classification with four classes produced a single class (27% of particles) that exhibited shape and features expected for this protein. Particles belonging to this 3D class were re-extracted and binned twice before an initial consensus 3D refinement (C1) was performed, which converged to 5.3 Å. After 3D refinement, the particle stack was further separated using 3D classification in RELION-3.0 using the consensus map filtered to 30 Å as a model and using local angular searches and higher Tau-factor (*T*) values (*T* = 8), subdividing into a further four classes. Of the four classes, three displayed over-fitted and noisy or broken features; however, a single class (39% of the input particles) showed clear secondary structure and internal features and was selected for further refinement. Particles corresponding to the best 3D classes were re-extracted (1.09 Å per pixel) and the remaining poor particles removed using 2D classification without alignment. The best classes were selected, resulting in a final particle stack of 132,193 images, which were refined by applying *C2* symmetry in RELION-3.0, according to the gold-standard refinement procedure. Beam-induced Bayesian particle polishing[61] followed by CTF refinement[59] was also performed, producing a final map of the Mec1–Ddc2 at 4.7 Å, according to the Fourier shell correlation (FSC) = 0.143 criterion, after post-processing in RELION-3.0 using a soft mask (*C2* symmetric) corresponding to the protein. Auto-refinement of the same particles in cisTEM[62], using the 4.7-Å reconstruction filtered to 20 Å as a starting model, produces a 4.3-Å map with features consistent with such estimates. The reconstructed volume was slightly larger than that obtained for the wild type bound with nucleotide (see below), suggesting an inaccurate pixel size. Therefore, the volume was scaled to match the volume of the nucleotide-bound reconstruction, with a pixel size of 1.05 Å per pixel producing a closely matched

structure. The numbers of particles and processing steps are summarized in Extended Data Fig. 3. Local resolution estimates calculated using ResMap[63] showed a resolution range of 3.5–5.5 Å. Angular distribution plots suggest that, while there are predominant views, rare views were captured by omitting initial 2D classification steps and tilting also circumvented the severity of the preferential orientation issues as confirmed by directional FSC plots[64].

Cryo-EM image processing of AMP-PNP-bound wild-type and F2244L datasets. Movie frames were processed analogously to the wild-type dataset except that the super-resolution images were twice binned, and gain corrected as part of the MotionCor2 processing step in RELION-3.0. CTF fitting was performed using CTFFIND4 (ref. [65]). Particles were picked with Gautomatch using the same templates as for the wild-type dataset and extracted using RELION-3.0 with a box size of 328×328 pixels and down sampled four times for initial processing. Again, 3D classification was initially performed with a Mec1–Ddc2 map[13,14] filtered to 60 Å. Data processing for Mec1–Ddc2–AMP-PNP followed a similar pipeline to that described for the apo structure (above), and also exhibited preferential orientation. However, careful classification using 2D and 3D approaches in RELION-3.0 was used to balance the views to counter the preferential orientation and to prevent anisotropic reconstructions that were difficult to interpret. Due to the relatively rare high-resolution front views (those that are described as butterfly in shape), the number of particles used in the final reconstruction was comparatively low compared with the dataset size. These particles were subjected to particle polishing and CTF refinement in RELION-3.0, resulting in a 4-Å-resolution reconstruction when refined in RELION-3.0 according to the gold-standard refinement procedure and applying $C2$ symmetry. Auto-refinement of the same particle stack in cisTEM, using the 20-Å filtered map as a starting model, produces a 3.8-Å reconstruction (FSC = 0.143). The numbers of particles and processing steps are summarized in Extended Data Fig. 3. Local resolution estimates were calculated using ResMap[63] and showed a resolution range of 3.5–4.5 Å. Angular distribution plots suggest that, while there are predominant views, carefully curating the particle stack maintained the rare views.

The Mec1(F2244L)–Ddc2–AMP-PNP data were preprocessed as described above (summarized in Extended Data Fig. 5). Initial 3D classification with four classes produced a single good class (47% of particles). Particles belonging to this good 3D class were re-extracted, twice binned and used in a consensus 3D refinement (C1) that converged to 4.3 Å. A 3D classification in RELION-3.0, using local angular searches with a starting map filtered to 30 Å and separating into four classes, produced a single main class (52%) exhibiting clear secondary structure features. Particles belonging to this major class were re-extracted, unbinned and refined, imposing $C2$ symmetry followed by per particle defocus refinement in RELION-3.0. Further separation to reach high resolution was achieved by 3D classification using higher T values ($T=8$) and subdividing into six classes, without alignment. Four of the six classes showed features consistent with Mec1–Ddc2 and were each refined by gold-standard 3D refinement in RELION, with two of the classes reaching ~8-Å (44% class) resolution or worse (21% class) as determined by the FSC = 0.143 criterion—suggesting that these were poor-quality particles. Two other classes could be refined separately to high resolution, with particle polishing and three rounds of CTF refinement, resulting in reconstructions approaching 3 Å when refined in RELION-3.0 according to the gold-standard refinement procedure and applying $C2$ symmetry. Auto-refinement of the same particle stacks in cisTEM, using the best reconstruction filtered to 20 Å as a starting model, produces a 2.8-Å reconstruction (FSC = 0.143, which we denote as State I; see main text for details), with features consistent with such estimates (Extended Data Figs. 6 and 7), and a 3.2-Å reconstruction (FSC = 0.143, which we denote as State II; see main text for details). We also refined the highest-resolution particles without symmetry ($C1$), which converged to 2.9-Å resolution (FSC = 0.143) and showed no major overall differences. However, the side-chain details in the active site of the C1 map were not as well defined, which we presume is due to some residual plasticity in the active site, as shown by the presence of States I and II in our dataset. The numbers of particles and processing steps are summarized in Extended Data Fig. 5. Local resolution estimates were calculated using ResMap[63] and showed a resolution range of 2.5–3.7 Å for State I map, and 2.7–4.3 Å for State II map. Angular distribution plots of both of the reconstructions show that this mutant sample does not suffer from severe preferential orientation despite being prepared in an analogous manner to the wild-type sample.

Model building and refinement. For map interpretation, reconstructions were blurred or sharpened using a range of positive or negative B-factors using MRCtoMTZ in CCPEM[66] to find optimum values of sharpening. The final wild-type maps were sharpened with a B-factor of −40 to −200 Å^2, and the F2244L reconstructions were sharpened using a of −20 to −60 Å^2. The high-resolution maps permitted accurate model building and therefore the structure was built manually using Coot[67], starting with the C-terminal kinase domain bound to AMP-PNP and using the high-resolution nucleotide-bound X-ray structures of mTOR[5,19,20] and EM structures of Mec1 (ref. [27]) and Tel1 (ref. [21]) as guides. We also built Ddc2 manually using the Ddc2 chain from the previously determined Mec1–Ddc2 structure (Protein Data Bank (PDB) 5X6O) docked into the destiny. We were

able to build coordinates with the majority of side chains corresponding to Mec1 (UNIPROT accession code P38111) and the majority (residue 189 to C terminus) of Ddc2 (UNIPROT accession code Q04377). The coordinates for the Mec1–Ddc2 dimer model were real-space refined in PHENIX[68,69] against the 2.8-Å map (sharpened with a B-factor of −30 Å^2). Refinements were limited to resolutions estimated by cisTEM (at FSC = 0.143) to prevent over-fitting. Ramachandran, C_β, noncrystallographic symmetry and secondary structure restraints (generated in PHENIX) were imposed throughout the refinement to ensure good model geometry; typically, three cycles of real-space refinement were run (three macro cycles of global and local optimization and B-factor refinement). PHENIX automatically estimates the relative weighting of the restraints and map to prevent over-fitting with each cycle and we re-ran real-space refinement using the best weighting value. The refined coordinates were validated using MOLPROBITY[70] within PHENIX, and manually adjusted in Coot before re-refinement. The Mec1(F2244L)–Ddc2 model (refined at 2.8 Å) was fitted into the 3.2-Å State II map (sharpened using a B-factor of −30 Å^2) and real-space refined in PHENIX using the same procedure as outlined above. The Mec1(F2244L)–Ddc2 model was fitted into the Mec1–Ddc2:AMP-PNP map at 3.8 Å (sharpened using a B-factor of −60 Å^2) and real-space refined in PHENIX using up to ten macro cycles in the first instance, due to the conformational changes between the two structures. The model was rebuilt in places that showed greater differences, such as the activation loop and PRD in the kinase domain. This was subjected to further real-space refinements in PHENIX analogous to the mutant structures. Refinement and model statistics are given in Table 1. Map versus model FSC curves were also generated for all structures in PHENIX as part of the refinement procedure and are given in Extended Data Figs. 4 and 6.

Model interpretation and analysis. Figures were created in PyMOL (Schrodinger), UCSF Chimera[71] and Chimera X[72]. Structural superpositions were performed in PyMOL. To analyze kinase domain differences, kinase domains were aligned to the catalytic loop. For dimer interface differences, the structures were aligned to a single promoter of Mec1–Ddc2. Interface buried surface area estimates were calculated using PISA[73].

Quantification and statistical analysis. Cryo-EM data were analyzed and quantified using a Bayesian approach as described in RELION[59,74]. No statistical methods were used to predetermine sample size, except sufficient images were collected to ensure that adequate reconstructions could be obtained.

Reporting Summary. Further information on research design is available in the Nature Research Reporting Summary linked to this article.

Data availability
The cryo-EM reconstruction volumes and the atomic coordinates generated in this study are available at the EMDB under accession codes EMD-11050 (nucleotide-bound F2244L mutant State I), EMD-11051 (nucleotide-bound F2244L mutant State II), EMD-11055 (nucleotide-bound wild type) and EMD-11056 (wild type); and the RCSB Protein Data Bank under the PDB codes 6Z2W (AMP-PNP-bound F2244L State I), 6Z2X (AMP-PNP-bound F2244L State II) and 6Z3A (AMP-PNP-bound wild type). Yeast strains, plasmids and plasmid sequences are available upon request. Source data are provided with this paper.

References
53. McDonald, J. P., Levine, A. S. & Woodgate, R. The *Saccharomyces cerevisiae* RAD30 gene, a homologue of *Escherichia coli dinB* and *umuC*, is DNA damage inducible and functions in a novel error-free postreplication repair mechanism. *Genetics* **147**, 1557–1568 (1997).
54. Zhao, X., Muller, E. G. & Rothstein, R. A suppressor of two essential checkpoint genes identifies a novel protein that negatively affects dNTP pools. *Mol. Cell* **2**, 329–340 (1998).
55. Chabes, A., Domkin, V. & Thelander, L. Yeast Sml1, a protein inhibitor of ribonucleotide reductase. *J. Biol. Chem.* **274**, 36679–36683 (1999).
56. Hailemariam, S. et al. The telomere-binding protein Rif2 and ATP-bound Rad50 have opposing roles in the activation of yeast Tel1^{ATM} kinase. *J. Biol. Chem.* **294**, 18846–18852 (2019).
57. Hustedt, N. & Shimada, K. Analyzing DNA replication checkpoint in budding yeast. *Methods Mol. Biol.* **1170**, 321–341 (2014).
58. Zheng, S. Q. et al. MotionCor2: anisotropic correction of beam-induced motion for improved cryo-electron microscopy. *Nat. Methods* **14**, 331–332 (2017).
59. Zivanov, J. et al. New tools for automated high-resolution cryo-EM structure determination in RELION-3. *Elife* **7**, e42166 (2018).
60. Zhang, K. Gctf: real-time CTF determination and correction. *J. Struct. Biol.* **193**, 1–12 (2016).
61. Zivanov, J., Nakane, T. & Scheres, S. H. W. A Bayesian approach to beam-induced motion correction in cryo-EM single-particle analysis. *IUCrJ* **6**, 5–17 (2019).

62. Grant, T., Rohou, A. & Grigorieff, N. cisTEM, user-friendly software for single-particle image processing. *Elife* **7**, e35383 (2018).

63. Kucukelbir, A., Sigworth, F. J. & Tagare, H. D. Quantifying the local resolution of cryo-EM density maps. *Nat. Methods* **11**, 63–65 (2014).

64. Tan, Y. Z. et al. Addressing preferred specimen orientation in single-particle cryo-EM through tilting. *Nat. Methods* **14**, 793–796 (2017).

65. Rohou, A. & Grigorieff, N. CTFFIND4: fast and accurate defocus estimation from electron micrographs. *J. Struct. Biol.* **192**, 216–221 (2015).

66. Burnley, T., Palmer, C. M. & Winn, M. Recent developments in the *CCP-EM* software suite. *Acta Crystallogr. D Struct. Biol.* **73**, 469–477 (2017).

67. Emsley, P. & Cowtan, K. *Coot*: model-building tools for molecular graphics. *Acta Crystallogr. D Biol. Crystallogr.* **60**, 2126–2132 (2004).

68. Afonine, P. V. et al. New tools for the analysis and validation of cryo-EM maps and atomic models. *Acta Crystallogr. D Struct. Biol.* **74**, 814–840 (2018).

69. Adams, P. D. et al. *PHENIX*: a comprehensive Python-based system for macromolecular structure solution. *Acta Crystallogr. D Biol. Crystallogr.* **66**, 213–221 (2010).

70. Chen, V. B., Wedell, J. R., Wenger, R. K., Ulrich, E. L. & Markley, J. L. MolProbity for the masses—of data. *J. Biomol. NMR* **63**, 77–83 (2015).

71. Pettersen, E. F. et al. UCSF Chimera—a visualization system for exploratory research and analysis. *J. Comput. Chem.* **25**, 1605–1612 (2004).

72. Goddard, T. D. et al. UCSF ChimeraX: meeting modern challenges in visualization and analysis. *Protein Sci.* **27**, 14–25 (2018).

73. Krissinel, E. & Henrick, K. Inference of macromolecular assemblies from crystalline state. *J. Mol. Biol.* **372**, 774–797 (2007).

74. Scheres, S. H. RELION: implementation of a Bayesian approach to cryo-EM structure determination. *J. Struct. Biol.* **180**, 519–530 (2012).

Author contributions

E.A.T., L.A.Y., X.Z. and P.M.B. planned this study. E.A.T. carried out the biochemical and genetic studies. L.A.Y. carried out the structural studies. All authors were involved in the interpretation of the results and the writing of the paper and approved the final version.

Competing interests

The authors declare no competing interests.

Additional information

Extended data is available for this paper at https://doi.org/10.1038/s41594-020-00522-0.

Supplementary information is available for this paper at https://doi.org/10.1038/s41594-020-00522-0.
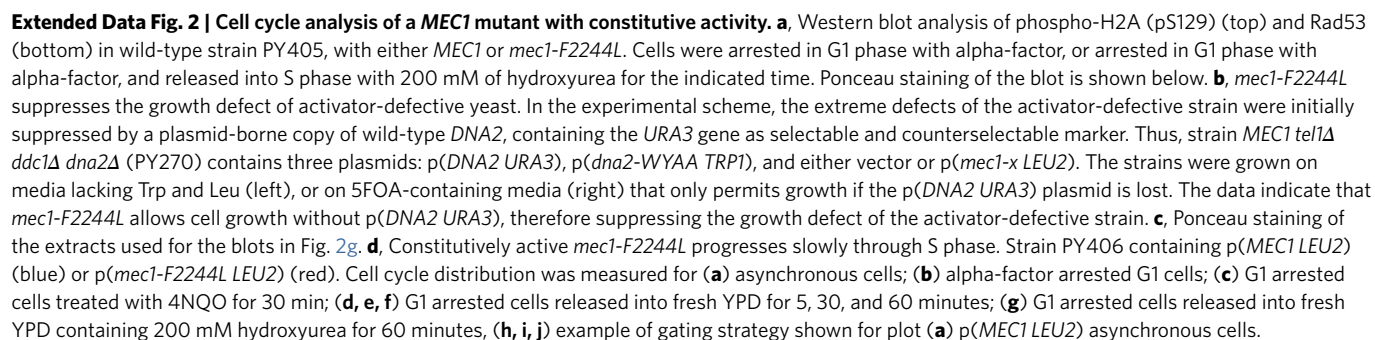
Correspondence and requests for materials should be addressed to X.Z. or P.M.B.
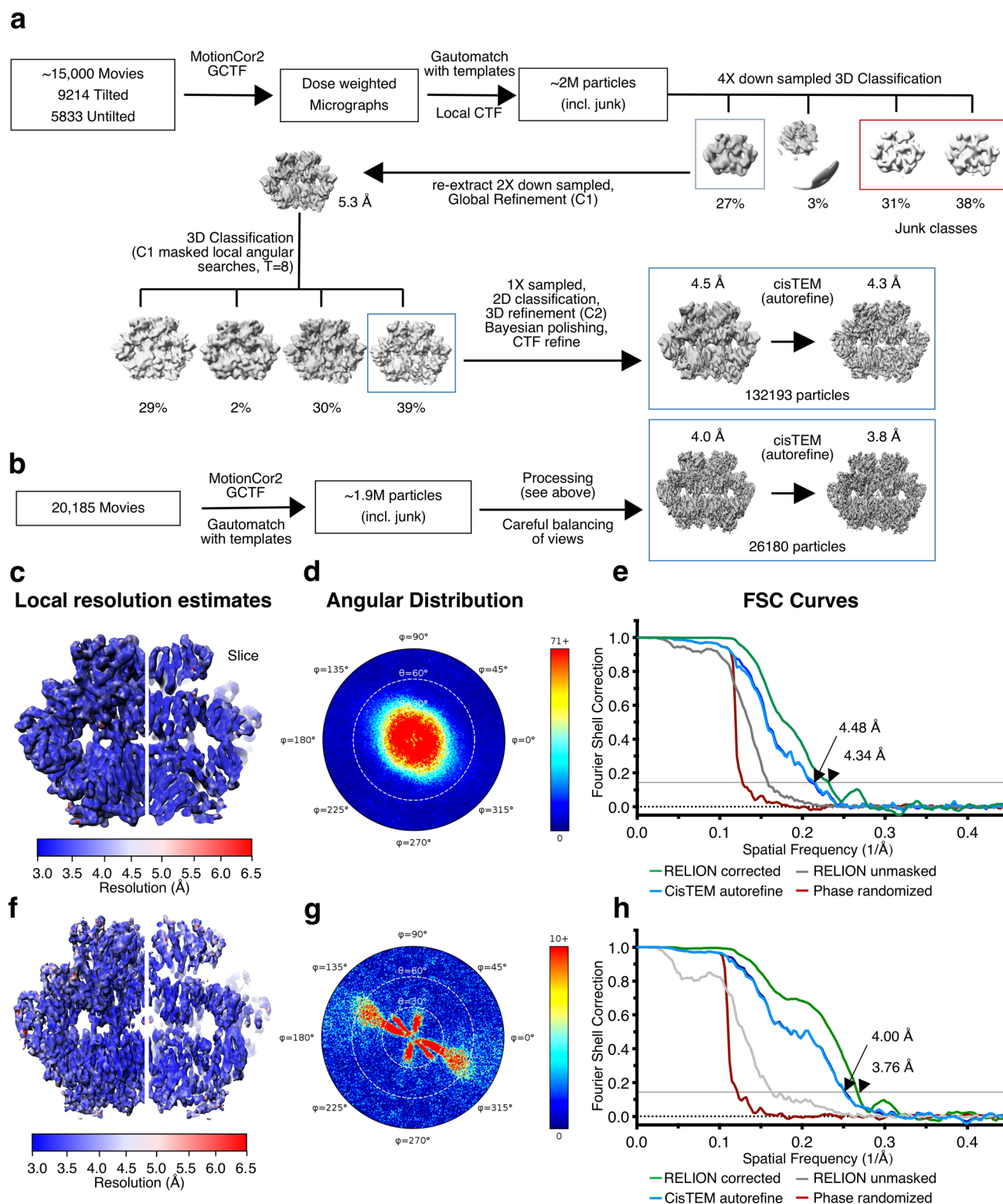
Peer review information Peer reviewer reports are available. Beth Moorefield was the primary editor on this article and managed its editorial process and peer review in collaboration with the rest of the editorial team.

**Reprints and permissions information** is available at www.nature.com/reprints.
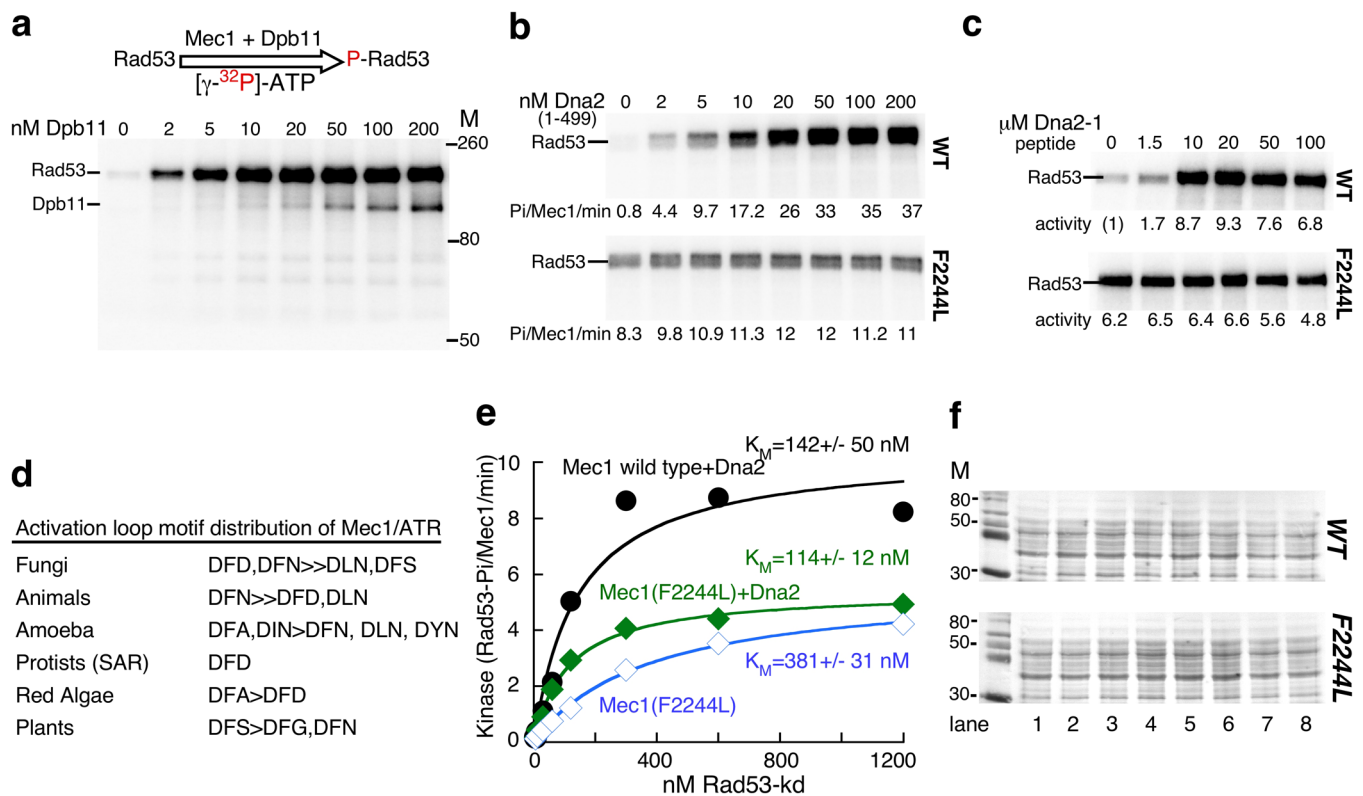
Extended Data Fig. 1 | Activation loop mutagenesis of Mec1. a, Representative complete gel of Mec1 kinase assay, described in Fig. 2. The gel shown is for the experiment in Fig. 2a, WT. **b**, Kinase activity of Mec1 and Mec1(F2244L) as a function of Dna2(1-499). Phosphorylation rates are given below the gel. **c**, Kinase activity of Mec1 and Mec1(F2244L) as a function of Dna2-1 peptide: HHDFTQDEDGPMEEVIWKYSPLQRDMSDKT. Fold stimulation compared to wild-type Mec1 without activator is given. **d**, Phylogenetic analysis of the activation loop [2243]DFD[2245] motif. 640 eukaryotic Mec1/ATR sequences were aligned with MSAProbs (https://toolkit.tuebingen.mpg.de/), filtered to a set of 95 sequences that showed less than 50% sequence identity, and the motif distribution recorded. **e**, Titration of Rad53 into the Mec1 assay. Standard assays with 3 nM Mec1 and 5 nM Dna2(1-499) activator, or with 3 nM Mec1(F2244L) with or without 5 nM Dna2(1-499) activator were carried out at increasing concentrations of GST-Rad53-kd. Activities are expressed as Rad53 phosphates per Mec1 (monomer) per minute, and the data were modeled to the Michaelis-Menten equation. **f**, Ponceau staining of the extracts used for the Western blots in Fig. 2e.

Extended Data Fig. 2 | Cell cycle analysis of a *MEC1* mutant with constitutive activity. a, Western blot analysis of phospho-H2A (pS129) (top) and Rad53 (bottom) in wild-type strain PY405, with either *MEC1* or *mec1-F2244L*. Cells were arrested in G1 phase with alpha-factor, or arrested in G1 phase with alpha-factor, and released into S phase with 200 mM of hydroxyurea for the indicated time. Ponceau staining of the blot is shown below. **b**, *mec1-F2244L* suppresses the growth defect of activator-defective yeast. In the experimental scheme, the extreme defects of the activator-defective strain were initially suppressed by a plasmid-borne copy of wild-type *DNA2*, containing the *URA3* gene as selectable and counterselectable marker. Thus, strain *MEC1 tel1Δ ddc1Δ dna2Δ* (PY270) contains three plasmids: p(*DNA2 URA3*), p(*dna2-WYAA TRP1*), and either vector or p(*mec1-x LEU2*). The strains were grown on media lacking Trp and Leu (left), or on 5FOA-containing media (right) that only permits growth if the p(*DNA2 URA3*) plasmid is lost. The data indicate that *mec1-F2244L* allows cell growth without p(*DNA2 URA3*), therefore suppressing the growth defect of the activator-defective strain. **c**, Ponceau staining of the extracts used for the blots in Fig. 2g. **d**, Constitutively active *mec1-F2244L* progresses slowly through S phase. Strain PY406 containing p(*MEC1 LEU2*) (blue) or p(*mec1-F2244L LEU2*) (red). Cell cycle distribution was measured for (**a**) asynchronous cells; (**b**) alpha-factor arrested G1 cells; (**c**) G1 arrested cells treated with 4NQO for 30 min; (**d, e, f**) G1 arrested cells released into fresh YPD for 5, 30, and 60 minutes; (**g**) G1 arrested cells released into fresh YPD containing 200 mM hydroxyurea for 60 minutes, (**h, i, j**) example of gating strategy shown for plot (**a**) p(*MEC1 LEU2*) asynchronous cells.

a

b

c
Local resolution estimates

d
Angular Distribution

e
FSC Curves

f

g

h

Extended Data Fig. 3 | CryoEM processing and reconstruction quality of Mec1-Ddc2. a, b, Processing tree resulting reconstructions of Mec1-Ddc2 and a second reconstruction in complex with AMP-PNP (see Methods for details). **c, f**, Local resolution estimates from ResMap, with slice through the density to show internal features, of apo (**c**) and bound with AMP-PNP (**f**). **d, g**, Angular distribution from CisTEM autorefine, and (**e, h**) Gold-standard Fourier shell correlation (FSC) from RELION-3.0 and CisTEM.
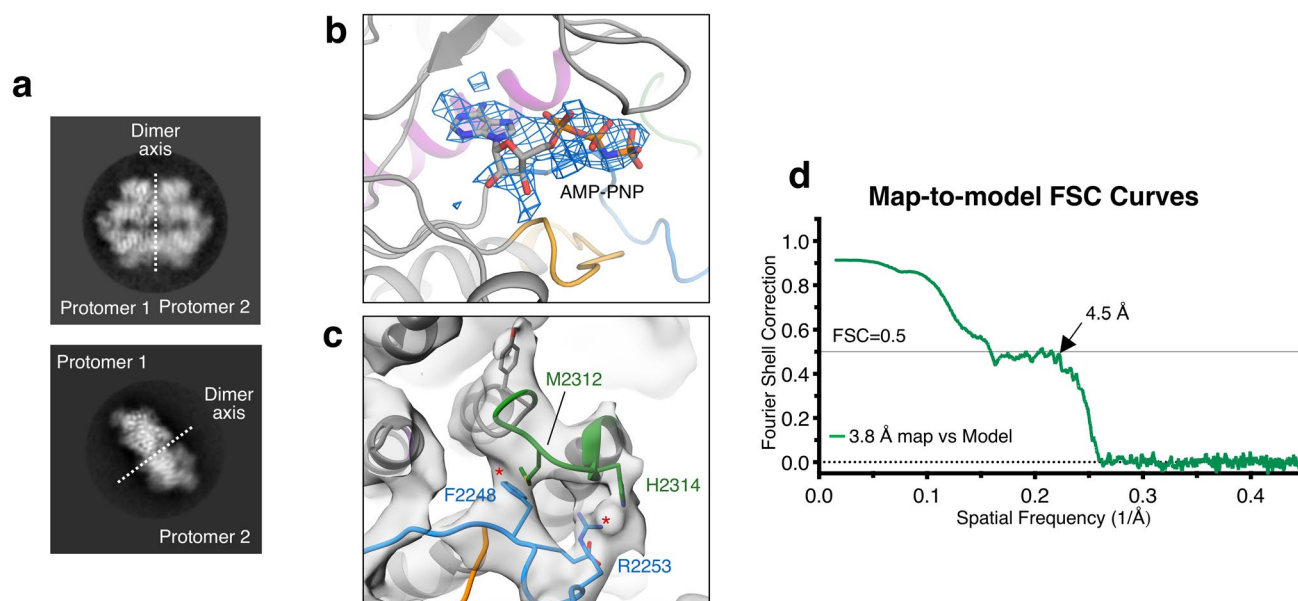
Extended Data Fig. 4 | Map and model features of the Mec1-Ddc2 complex. a, 2D classes of Mec1-Ddc2 after a focused 3D refinement masking on Mec1-Ddc2 heterodimer, showing intrinsic flexibility of the complex across the dimer interface. **b**, Electron density features of the bound AMP-PNP, and **c**, strong electron density (unsharpened map) showing the PRD-I interaction with the activation loop at two points (asterisked). **d**, Map to model FSC curves.
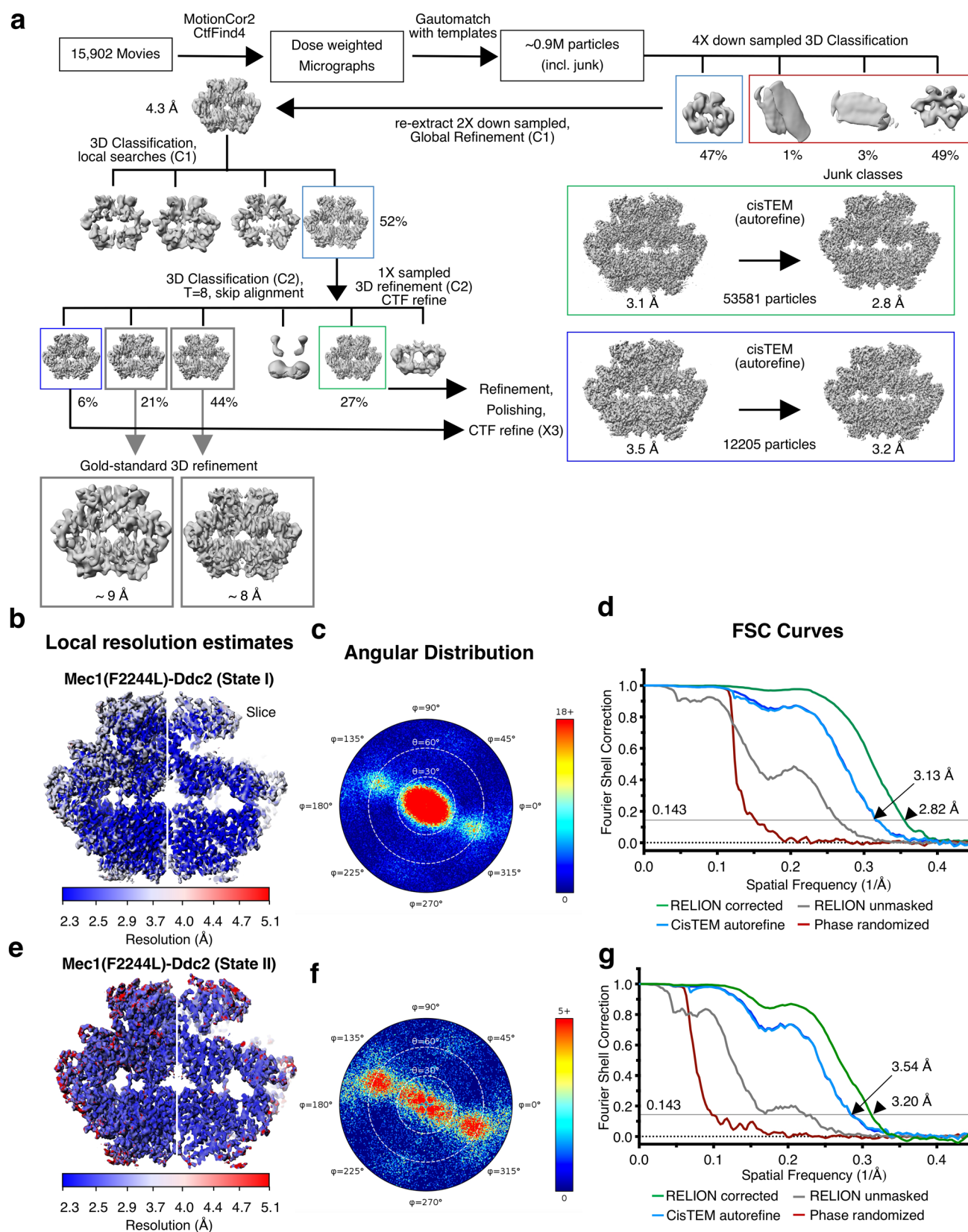
Extended Data Fig. 5 | CryoEM processing and reconstruction quality of Mec1(F2244L)-Ddc2. a, Processing tree resulting in high resolution reconstructions of Mec1(F2244L)-Ddc2 in complex with AMP-PNP and magnesium captured in two states (see Methods). **b**, Local resolution estimates from ResMap, with slice through the density to show internal features, of State I, (**c**) angular distribution from CisTEM autorefine, and (**d**) Gold-standard Fourier shell correlation (FSC) from RELION-3.0 and CisTEM. **e**, Local resolution estimates from ResMap of State II, with (**f**) angular distribution from CisTEM autorefine, and (**g**) Gold-standard Fourier shell correlation (FSC) from RELION-3.0 and CisTEM.
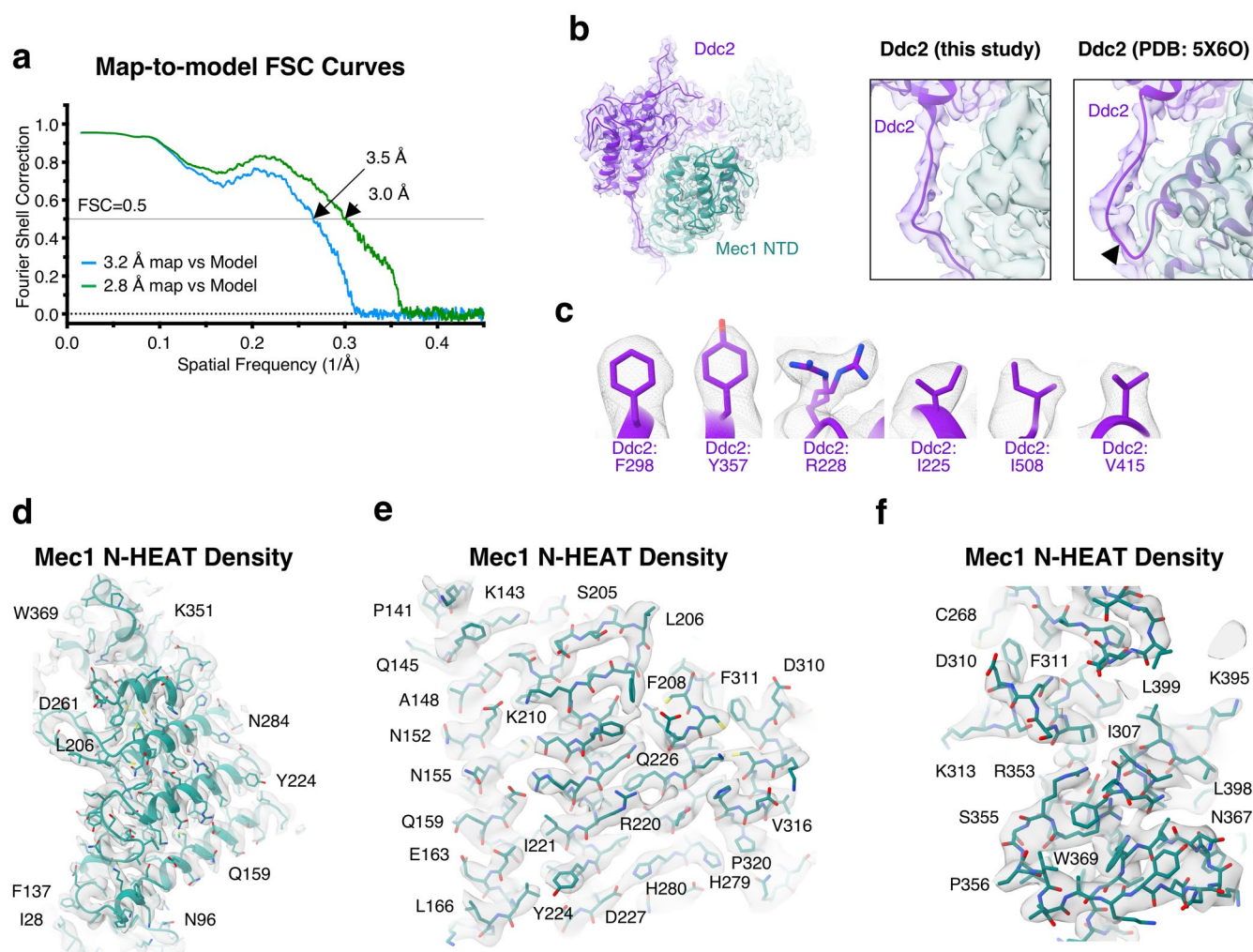
Extended Data Fig. 6 | Data and model quality of the Mec1(F2244L)-Ddc2 reconstruction. a, Map to model FSC curves of the F2244 mutant reconstruction. **b**, Ddc2 and Mec1 N-terminal domain density (NTD) and model showing clear separation of Mec1 and Ddc2 proteins for accurate model building of this region (*left*), with close-up views of chain tracing between the model built in this study (*middle*) and the previously published model (PDB:5X6O) (*right*). The arrow indicates the point at which the two models diverge. **c**, High-resolution features from the 2.8 Å map, showing that the electron density quality is sufficient to resolve types of aromatic residues (Phenylalanine over Tyrosines), β−branched side chains (Isoleucine), as well as smaller hydrophobics (Valine) and an example of a split conformation of Arginine. **d-f**, CryoEM density regions of the Mec1 N-terminal domain (~300 amino acids) showing the overall fit of the model and side chains (labeled), along with close-up views of different regions showing unambiguous side chain density for accurate model building.
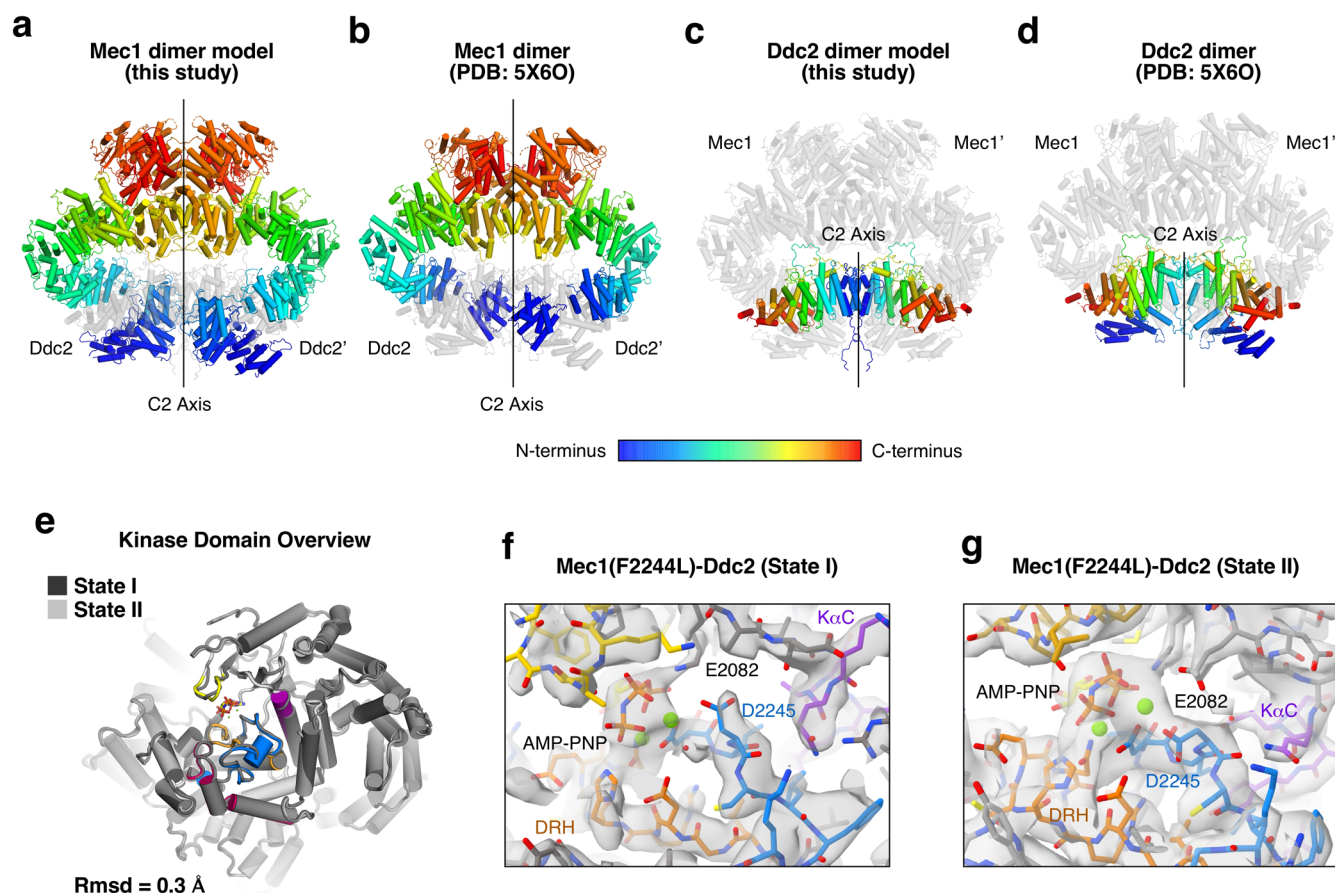
Extended Data Fig. 7 | Global and kinase domain structural comparisons of Mec1-Ddc2. a-d, Structural comparisons between the Mec1 model (**a,b**) and Ddc2 model (**c,d**) from this study and the PDB:5X6O showing the global differences in N-terminal domains of both proteins. **e-g,** Overall comparison between the kinase region of Mec1(F2244L) State I (gray) and State II (light gray), demonstrating that both states are very similar outside of the active site with an Rmsd = 0.3 Å. **f-g,** Electron density of the nucleotide binding site and different side chain conformations associated with State I and State II (see main text for details).
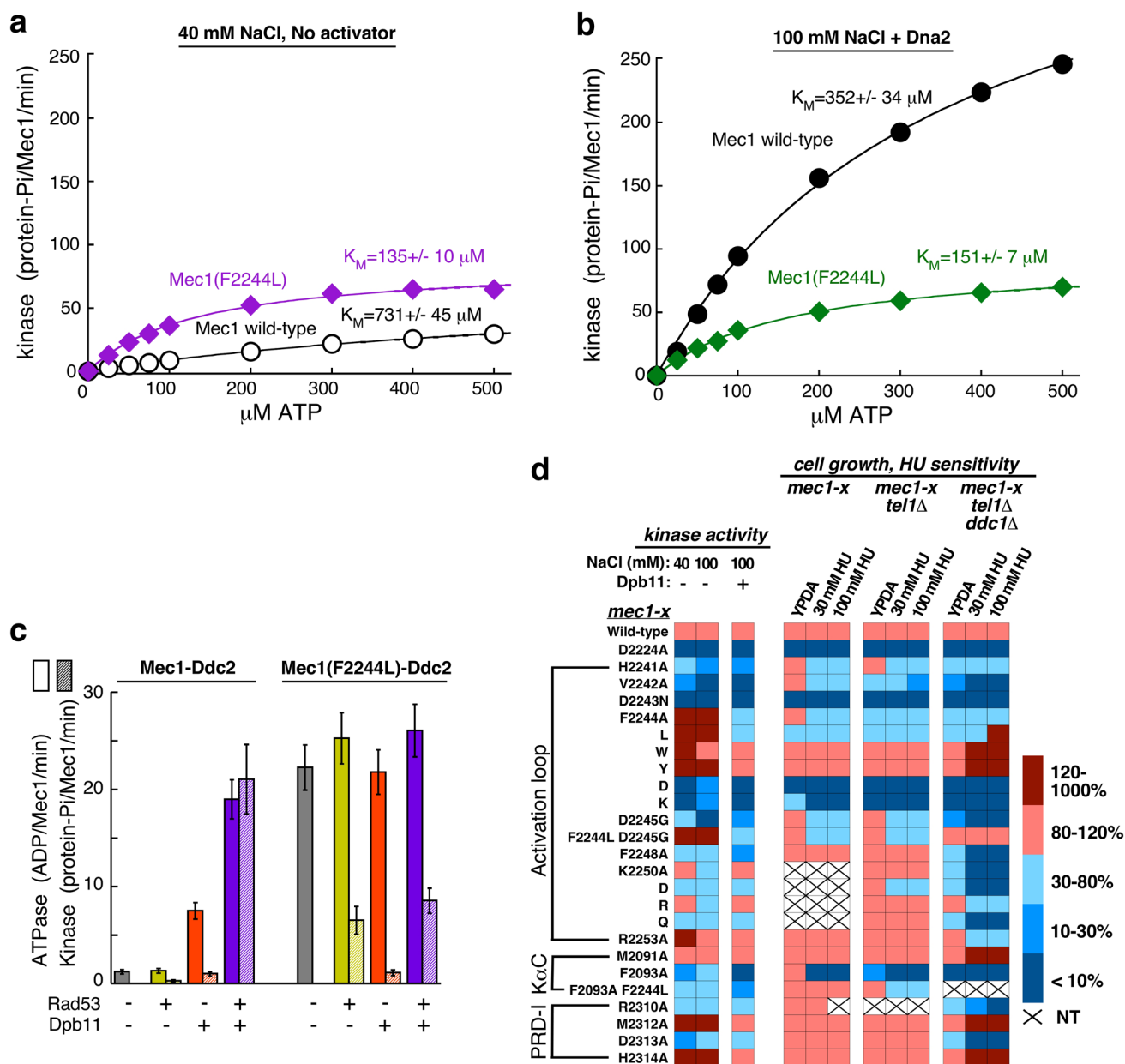
Extended Data Fig. 8 | ATP dependence of Mec1 activity. a, Standard Mec1 kinase assays without activator at 40 mM NaCl, or (**b**) with 200 nM Dna2(1-499) at 100 mM NaCl, were carried out at increasing concentrations of ATP. Activities are expressed as protein phosphates (Rad53 plus Dna2(1-499) when relevant) per Mec1 (monomer) per minute. **c**, Comparative ATPase (solid bars) and kinase (striped bars) activities of Mec1-Ddc2 and Mec1(F2244L)-Ddc2, in the presence or absence of Rad53 and Dpb11 (see Methods). **d**, Summary of phenotypes of all Mec1 mutants. The *in vitro* and *in vivo* phenotypes of the mutants are shown in the form of heat maps using Prism 8 GraphPad software.
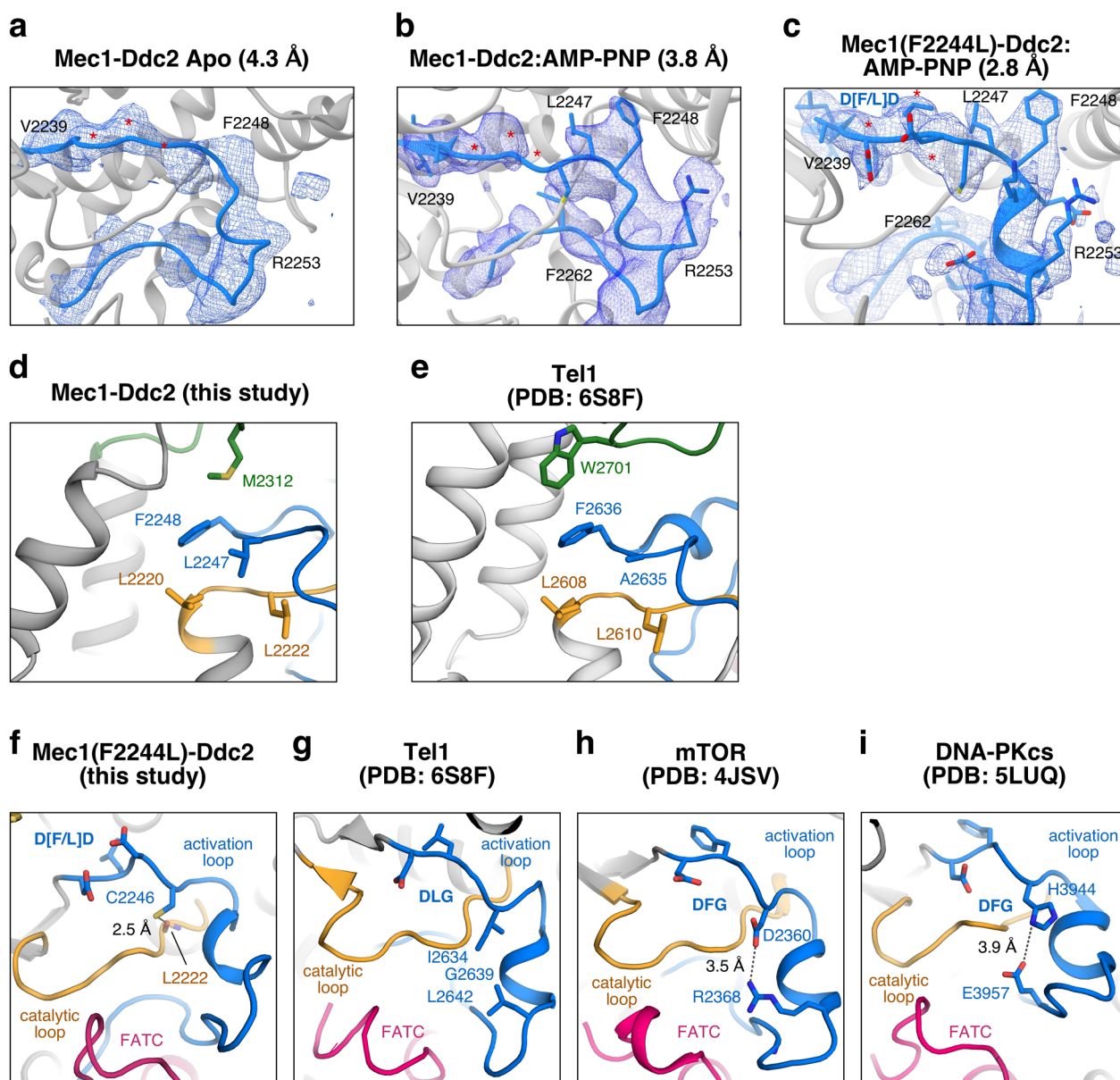
Extended Data Fig. 9 | Structural analysis and comparisons of Mec1. a-c, Electron density of the activation loop from the apo (**a**), AMP-PNP-bound (**b**) and AMP-PNP-bound F2244L mutant (**c**), showing that in all cases the activation loop remains ordered, with flexibility around the DFD-motif (asterisks), which could not be easily resolved in the wild-type structures. Several large residues are shown as landmarks. **d,e**, PRD-I hydrophobic network comparisons between Mec1-Ddc2 (**e**) and Tel1 (**e**), suggesting that M2312 plays an analogous role to W2701 in Tel1. PRD-I, activation loop and catalytic loop are colored as in Fig. 1b. **f-i**, Comparison of stabilizing interactions in activations loops across PIKKs. **f**, In Mec1, the DFD+1 residue plays a role in stabilizing the activation loop. In our activated structure the thiol group of the invariant C2246 forms an H-bond with the main chain carbonyl of L2222 of the catalytic loop, helping to stabilize the active state. In Tel1 the DLG+1 (I2634) forms a hydrophobic spline with G2639 and L2642 of the activation loop (**g**), whereas in mTOR (**h**) and DNA-PKcs (**i**) an ion pair is preferred.

Corresponding author(s): Peter M Burgers, Xiaodong Zhang

Last updated by author(s): Sep 10, 2020

Reporting Summary

Nature Research wishes to improve the reproducibility of the work that we publish. This form provides structure for consistency and transparency in reporting. For further information on Nature Research policies, see our Editorial Policies and the Editorial Policy Checklist.

Statistics

For all statistical analyses, confirm that the following items are present in the figure legend, table legend, main text, or Methods section.

n/a	Confirmed	
☐	☒	The exact sample size (*n*) for each experimental group/condition, given as a discrete number and unit of measurement
☐	☒	A statement on whether measurements were taken from distinct samples or whether the same sample was measured repeatedly
☒	☐	The statistical test(s) used AND whether they are one- or two-sided *Only common tests should be described solely by name; describe more complex techniques in the Methods section.*
☐	☒	A description of all covariates tested
☒	☐	A description of any assumptions or corrections, such as tests of normality and adjustment for multiple comparisons
☐	☒	A full description of the statistical parameters including central tendency (e.g. means) or other basic estimates (e.g. regression coefficient) AND variation (e.g. standard deviation) or associated estimates of uncertainty (e.g. confidence intervals)
☒	☐	For null hypothesis testing, the test statistic (e.g. *F*, *t*, *r*) with confidence intervals, effect sizes, degrees of freedom and *P* value noted *Give P values as exact values whenever suitable.*
☒	☐	For Bayesian analysis, information on the choice of priors and Markov chain Monte Carlo settings
☒	☐	For hierarchical and complex designs, identification of the appropriate level for tests and full reporting of outcomes
☒	☐	Estimates of effect sizes (e.g. Cohen's *d*, Pearson's *r*), indicating how they were calculated

Our web collection on statistics for biologists contains articles on many of the points above.

Software and code

Policy information about availability of computer code

Data collection	EPU 2 Software (ThermoFisher), BD CellQuest Pro
Data analysis	MotionCorr2, Gautomatch, GCTF, CTFFind4, RELION-3.0, CisTEM, COOT, Phenix, MolProbity, UCSF Chimera, ChimeraX, PyMol, Prism 8, Kaleidagraph, flowJo, Jalview

For manuscripts utilizing custom algorithms or software that are central to the research but not yet described in published literature, software must be made available to editors and reviewers. We strongly encourage code deposition in a community repository (e.g. GitHub). See the Nature Research guidelines for submitting code & software for further information.

Data

Policy information about availability of data

All manuscripts must include a data availability statement. This statement should provide the following information, where applicable:

- Accession codes, unique identifiers, or web links for publicly available datasets
- A list of figures that have associated raw data
- A description of any restrictions on data availability

The cryoEM reconstruction volumes and the atomic coordinates generated in this study are available at the EMDB under accession code EMD-11050 (nucleotide-bound F2244L mutant State I), EMD-11051 (nucleotide-bound F2244L mutant State II), EMD-11055 (nucleotide-bound wild-type), EMD-11056 (wild-type), and the RCSB Protein Data Bank under the PDB codes 6Z2W (AMP-PNP-bound F2244L State I), 6Z2X (AMP-PNP-bound F2244L State II), 6Z3A (AMP-PNP-bound wild-type).

Field-specific reporting

Please select the one below that is the best fit for your research. If you are not sure, read the appropriate sections before making your selection.

☒ Life sciences   ☐ Behavioural & social sciences   ☐ Ecological, evolutionary & environmental sciences

For a reference copy of the document with all sections, see nature.com/documents/nr-reporting-summary-flat.pdf

Life sciences study design

All studies must disclose on these points even when the disclosure is negative.

Sample size	For cryoEM, no statistical methods were used to predetermine sample size except sufficient images were collected to ensure adequate reconstructions can be obtained.
Data exclusions	For cryoEM, no data were initially excluded from the analysis although final reconstructions were obtained from subset of the data as detailed in Methods and Extended Data. No biochemical data were excluded.
Replication	Yes. The protein sample quality was assessed by SDS-PAGE and SEC, as reported previously. Thousands of micrographs with each sample were consistent in quality. Several independent cryoEM datasets were used as well as different software which deal with large dataset in a statistically significant manner. The biochemical studies were carried in triplicate. The genetic studies were carried in triplicate.
Randomization	All data were used in an unbiased way for data analysis and image reconstruction. Final quality control (such as resolution estimation) were conducted by randomly separating data into two halves and to calculate their correlation coefficients.
Blinding	There are no bias or randomization involved in the analysis so blinding is not relevant to this type of study.

Reporting for specific materials, systems and methods

We require information from authors about some types of materials, experimental systems and methods used in many studies. Here, indicate whether each material, system or method listed is relevant to your study. If you are not sure if a list item applies to your research, read the appropriate section before selecting a response.

Materials & experimental systems

n/a	Involved in the study
☐	☒ Antibodies
☒	☐ Eukaryotic cell lines
☒	☐ Palaeontology and archaeology
☒	☐ Animals and other organisms
☒	☐ Human research participants
☒	☐ Clinical data
☒	☐ Dual use research of concern

Methods

n/a	Involved in the study
☒	☐ ChIP-seq
☐	☒ Flow cytometry
☒	☐ MRI-based neuroimaging

Antibodies

Antibodies used	Rabbit anti-Rad53 antibody, Abcam, ab104232, multiple lots Anti-histone H2A (phospho S129), Abcam, ab15083, multiple lots
Validation	Manufacturer's websites describe the reactivity species for both antibodies to Saccharomyces cerevisiae proteins, and provide relevant references.

Flow Cytometry

Plots

Confirm that:

☒ The axis labels state the marker and fluorochrome used (e.g. CD4-FITC).

☒ The axis scales are clearly visible. Include numbers along axes only for bottom left plot of group (a 'group' is an analysis of identical markers).

☒ All plots are contour plots with outliers or pseudocolor plots.

☒ A numerical value for number of cells or percentage (with statistics) is provided.

Methodology

Sample preparation	For cell cycle analysis, Saccharomyces cerevisiae cells were grown and synchronized in the desired phase. Cells were washed, treated with RNase A and proteinase K, then stained with propidium iodide. Before analysis, cells were sonicated and the content of ~30,000 cells were analyzed.
Instrument	FACS Calibur-3, BD Biosciences
Software	BD CellQuest Pro, FlowJo
Cell population abundance	~30,000 cells
Gating strategy	Yeast cells that are attached or clumped with data points >2n in size were excluded

☒ Tick this box to confirm that a figure exemplifying the gating strategy is provided in the Supplementary Information.